Evidence of a dual African and Australian biomass burning influence on the vertical distribution of aerosol and carbon monoxide over the Southwest Indian Ocean basin in early 2020

Nelson Bègue[1], Alexandre Baron[2,3], Gisèle Krysztofiak[4], Gwenaël Berthet[4], Hassan Bencherif[1,5], Corinna Kloss[4], Fabrice Jégou[4], Sergey Khaykin[6], Marion Ranaivombola[1], Tristan Millet[1], Thierry Portafaix[1], Valentin Duflot[1], Philippe Keckhut[6], Hélène Vérèmes[1], Guillaume Payen[7], Mahesh Kumar Sha[8], Pierre-François Coheur[9], Cathy Clerbaux[9,10], Michaël Sicard[1], Tetsu Sakai[11], Richard Querel[12], Ben Liley[12], Dan Smale[12], Isamu Morino[13], Osamu Ochino[11,13], Tomohiro Nagai[11], Penny Smale[12] and John Robinson[12]

[1] Laboratoire de l'Atmosphère et des Cyclones, UMR 8105 CNRS, Université de la Réunion, Reunion Island, France.

[2] Cooperative Institute for Research in Environmental Sciences (CIRES), University of Colorado, Boulder, CO 80305, USA

[3] NOAA Chemical Sciences Laboratory (CSL), 325 Broadway, Boulder, CO 80305, USA

[4] Laboratoire de Physique et Chimie de l'Environnement et de l'Espace (LPC2E), Université d'Orléans, CNRS UMR7328, Orléans, France.

[5] School of Chemistry and Physics, University of KwaZulu-Natal, Durban 4041, South Africa

[6] Laboratoire Atmosphères, Observations Spatiales (LATMOS), IPSL, UVSQ Université Paris-Saclay, Sorbonne Université, CNRS, Guyancourt, France

[7] Observatoire des Sciences de l'Univers de La Réunion (OSU-Réunion), UAR3365, Saint-Denis de la Réunion, France

[8] Royal Belgian Institute for Space Aeronomy (BIRA-IASB), Brussels, Belgium

[9] Université libre de Bruxelles (ULB), Spectroscopy, Quantum Chemistry and Atmospheric Remote Sensing (SQUARES), Brussels 1050, Belgium; Bruxelles (ULB), Brussels 1050, Belgium.

[10] Laboratoire Atmosphères, Observations Spatiales (LATMOS), IPSL, Sorbonne Université, UVSQ, CNRS, Paris, France

[11] Meteorological Research Institute, 1-1 Nagamine, Tsukuba, Ibaraki 305-0052, Japan

[12] National Institute of Water & Atmospheric Research (NIWA), Lauder, New Zealand

[13] National Institute for Environmental Studies, Tsukuba, Japan

1   Correspondence to: N.Bègue (nelson.begue@univ-reunion.fr)

2 **Abstract**

3   The pristine atmosphere of the southwest Indian Ocean (SWIO) basin underwent significant

4   perturbations during the 2020 austral summer. This study documents the complex variability of

5   aerosols and carbon monoxide (CO) over this remote oceanic region and identifies the processes

6   governing it in the upper troposphere – lower stratosphere (UT-LS). Aerosol profiles exhibit a

7   multi-layer structure in the tropical UT-LS in January and February 2020. The numerical

8   models (FLEXPART and MIMOSA) showed that the modulation of the aerosol content in the

9   lower stratosphere is due to the intense and persistent stratospheric aerosol smoke layer

10   generated during the 2019-20 extreme Australian bushfire events. One part of this stratospheric

11   aerosol smoke layer was advected zonally by the prevailing easterly winds and its passage over

12   Reunion was recorded by increased aerosol extinction profiles on 27th and 28th January. The

13   analysis of the advected potential vorticity highlights an isentropic transport of air masses

14   containing Australian biomass burning aerosol from extra-tropical latitudes to Reunion at the

15   400 K isentropic level, on 28th January. Interestingly, our results show that the BB activity in

16   eastern Africa, weak during this season, contributed to modulate (up to 90%) the vertical

17   distribution of CO and aerosols in the upper troposphere over the SWIO basin. The

18   simultaneous presence of African and Australian aerosols smoke layers has been recorded by

19   ground-based observations at Reunion. This study highlights for the first time the influence of

20   the African emissions from BB to the CO and aerosols distribution in the upper troposphere

21   over the SWIO basin during the convective season. The results show that besides PyroCb -

22   driven injection of BB products to the stratosphere, an alternative pathway may exist during the

23   regular deep-convection season in the tropics.

24   **1. Introduction**

25   Large amounts of aerosols and active trace gases such as carbon monoxide (CO) are injected

26   throughout the atmosphere during biomass burning (BB) events. The Southern American and

27   Southern African regions are recognized to be significant primary sources of carbonaceous

28   aerosols and active traces gases in the Southern Hemisphere through the BB season from July

29   to November (Bencherif et al., 2020; Garstang et al., 1996; Holanda et al., 2020). Such BB

30   activities have the potential to modulate the vertical distribution of trace gases and aerosols

31   from the troposphere to the stratosphere (Andreae and Merlet, 2001; Duflot et al., 2010; Héron

32   et al., 2020). Under favorable meteorological conditions, pyro-convection events can take place

33   and have the potential to inject soot and smoke directly into the stratosphere (Dowdy and Pepler,

34   2018; Fromm et al., 2010). Radiative impact of the aerosols and traces gases is determined by

1   abundance, vertical distribution, , and atmospheric residence time (which, in turn, will affect

2   the resultant horizontal distribution following advection (Darbyshire et al., 2018; Morgan et al.,

3   2019)). High concentrations of trace gases and aerosols from these fires can be transported far

4   from the source regions. This intercontinental transport has the potential to affect the

5   atmospheric composition of regions considered as aerosol-free areas.

6   The southwest Indian Ocean (SWIO) basin is known to be one of the few pristine regions on

7   Earth where the aerosol concentration is mainly governed by sea salts (Duflot et al., 2022). The

8   SWIO basin is characterized by a wet season (December to April) and a dry season (May to

9   November). Previous works showed that the atmospheric composition over the SWIO region

10   during the dry season is driven by the Southern Hemisphere BB activity (Clain et al., 2009;

11   Duflot et al., 2022; Edwards et al., 2006; Kaufman et al., 2003, Swap et al., 2003). These studies

12   pointed out that BB plumes cross South Africa during the dry season. Edwards et al. (2006)

13   revealed that southern African BB emissions mostly find their way into the SWIO basin and

14   follow the five transportation modes identified by Garstang et al. (1996). Being located in the

15   subtropical southern Indian Ocean at the crossroads of the transport pathway bringing air

16   masses from southern Africa, Reunion Island (21,0°S, 55.5°E) is a favorable location to study

17   the effect of this regional transport on atmospheric composition over the SWIO basin. Based

18   on ozone radiosonde and ground-based lidar observations recorded at Reunion, Clain et al.

19   (2009) highlighted a significant annual increase of tropospheric ozone over Reunion Island

20   during August-November period, in phase with the BB season in southern Africa and

21   Madagascar. High concentrations of ozone precursors from these fires are vented into the free

22   troposphere by convection and are subsequently advected into the SWIO basin by westerly

23   winds. In addition to regional transport, the tropical tropospheric composition over the SWIO

24   basin can be modulated by the long-range transport of BB plumes from South America (Duflot

25   et al., 2010, 2022; Zhou et al., 2018). By combining ground-based observations of Carbon

26   monoxide (CO) from a Fourier Transform Infrared (FTIR) spectrometer installed at Reunion

27   and the FLEXPART model simulations, Duflot et al. (2010) showed that southern African and

28   southern American BB events have the potential to inject large amounts of ozone precursors

29   such as CO and aerosols throughout the troposphere over the SWIO basin. The synergy of CO

30   and aerosols observations are helpful in discussions of the influence of BB events on the

31   evolution of the aerosol burden (Bègue et al., 2021; Bencherif et al., 2020; Jones et al., 2001).

32   Most recently, the analysis of Aerosols Optical Depth (AOD) recorded from sun-photometer at

33   Reunion over a period of 12-years has been undertaken by Duflot et al. (2022). Duflot et al.

34   (2022) showed that the BB activity explains 67 % of the variability of the AOD, within which

1 the contributions of the BB activity in Southern Africa and southern America are estimated at

2 22% and 20%, respectively. Although Australia is known for its intense BB events (Fromm et

3 al., 2006; 2010; De Laat et al., 2012), the contribution of the Australian BB activity on the

4 observed AOD variability over Reunion is relatively low (4.7 %).

5 The Australian BB activity takes mainly place in the northern part of the continent between

6 September and January (Russel-Smith et al., 2007). Nevertheless, the most disastrous fires burn

7 in the southeastern region of Australia. Extreme fires occurring over southeastern Australia

8 during the austral summer can lead to the development of pyro-convection events (Dowdy and

9 Pepler, 2018; Fromm et al., 2010). Southeastern Australia has a long history of severe pyro-

10 convection events which have significantly impacted the composition of the stratosphere at

11 regional and global scales. The last and largest event occurred during the 2019-20 fire season

12 (referred to as "Black Summer"). Previous works reported that this fire season is unrivaled with

13 a surface burnt estimated at 19 million hectares (Boer et al., 2020; Cai et al., 2022; Levin et al.,

14 2021). Furthermore, this extreme fire season can be considered as unprecedented due to

15 persistent planetary-scale perturbations induced in the stratosphere (Kablick et al., 2020;

16 Khaykin et al., 2020; Kloss et al., 2021; Ohneiser et al., 2020, 2022; Yu et al., 2020).

17 Kablick et al. (2020) showed at least 18 pyro-convection outbreaks occurred between 29th

18 December 2019 and 12th January 2020 with the largest event occurring around 1st January 2020.

19 Based on satellite observations and CESM-CARMA model results, Yu et al. (2021) showed

20 that Australian wildfires burning from December 2019 to January 2020 injected approximately

21 0.9 Tg of smoke into the stratosphere. The analysis of the numerical simulations suggest that

22 the smoke mass contained 2.5% black carbon which induced a 1 K warming in the stratosphere

23 of the Southern Hemisphere mid-latitude for more than 6 months following its injection. The

24 carbon-rich aerosol clouds were confined during their solar-driven rise by a persistent synoptic-

25 scale anticyclone (Kablick et al., 2020; Khaykin et al., 2020). As a consequence, the highly-

26 concentrated absorbing aerosols were lofted into the middle stratosphere, which prolongs their

27 stratospheric residence time and radiative effect on climate. The combustion products injected

28 into the stratosphere were advected by westerly winds and dispersed across all of the southern

29 hemisphere extra-tropical latitudes (Khaykin et al., 2020; Ohneiser et al., 2020, 2022; Tencé et

30 al., 2022; Yu et al., 2020). The stratospheric smoke layer was rapidly advected westward and

31 its optical characteristics were measured by the lidar system installed at Punta Arena (53.2°S,

32 70.9°E; Chile) and Rio Grandé (53.8° S, 67.7° W, Argentina) one week following its injection

33 (Ohneiser et al., 2022). Ohneiser et al. (2022) pointed out that the presence of the smoke layers

34 extended, on average, from 9 to 24 km in height, with one part ascending to more than 30 km

1   height as a result of self-lofting processes. The maximum smoke AOD was around 1.0 over

2   Punta Arenas in January 2020 and thus 2 to 3 orders of magnitude above the stratospheric

3   aerosol background of 0.005 (Ohneiser et al., 2022). Their results suggest an influence of this

4   stratospheric smoke layer on the record breaking ozone hole over Antarctica in September-

5   November 2020. This is consistent with the results reported by Tencé et al. (2022) from lidar

6   and ozonesondes measurements at the French Antarctic station Dumont d'Urville

7   (66.6°S,140.0°E). Tencé et al. (2022) pointed out the persistence of smoke aerosols in the

8   southern high-latitude stratosphere following the pyro-convection events. They also reported

9   that the 2020 stratospheric ozone depletion is above the decadal average at Dumont d'Urville.

10 The common point among these studies is their interest for the perturbation induced by the

11 2019-20 Australian fires on the stratospheric composition, and on the dynamical circulation

12 over the extra-tropical latitudes. In contrast, relatively little attention has been paid to the

13 perturbation induced by this Australian smoke layer over the tropical/subtropical latitudes.

14 This study has two aims: 1) document the transport of the Australian smoke layer in the southern

15 subtropics over Indian Ocean during the January-February period which correspond to the wet

16 season, and 2) to investigate the influence of Australian aerosol smoke layers on variability of

17 the aerosol optical properties and CO in the Upper Troposphere-Lower Stratosphere (UT-LS)

18 of the SWIO basin accounting for convective activity. Convective activity is more intense

19 during this season as the Inter-Tropical Convergence Zone (ITCZ) is present over the whole

20 basin (Lashkari et al., 2017). Furthermore, the convective activity is often synonym of tropical

21 depression which can reach the stage of tropical cyclone (Barthe et al., 2021; Neuman et al.,

22 1993). The Regional Specialized Meteorological Centre (RSMC) at Reunion reported that the

23 cyclonic season 2019-20 was characterized by the development of 6 tropical cyclones and 4

24 tropical storms in the SWIO basin.

25 The study is organized as follows: Section 2 describes the observations and the model used for

26 the investigation of the transport of the aerosol smoke layer. A review of the formation and the

27 transport of the Australian aerosol smoke layer over the Southern Hemisphere is provided in

28 Section 3. An analysis of the influence of the Australian aerosol smoke layer on the aerosol and

29 CO variability over the SWIO basin is given in Section 4. The discussion on the influence of

30 the convective activity on the transport of the aerosol smoke layer over the SWIO basin is

31 provided in Section 5. A summary and the perspectives of this study are given in Section 6.

32 **2. Instrumentation and Model description**

33   **2.1 Aerosols data sets**

1   The aerosol datasets used in this study resulted mainly from two ground-based observations

2   sites from the Network for the Detection of Atmospheric Composition Change (NDACC,

3   www.ndacc.org) network as well as a suite of spaceborne sensors products.

2.1.1 Lauder ground-based lidar

5   Aerosol optical properties measurements at Lauder (45.0°S; 169.7°E) have been performed

6   using lidars since 1992. A detailed description of the lidar system operating at Lauder is given

7   by Sakai et al. (2016), and it is summarized hereafter. The emitter system consists of a Nd:YAG

8   laser beam at 532 nm and is linearly polarized. The lidar detects Rayleigh-Mie backscattering

9   at 532 nm with parallel and perpendicular components. The methodology described by Fernald

10   et al. (1984) is used to obtain the extinction and backscatter coefficient from a Rayleigh-Mie

11   lidar. This methodology involves the use of an extinction-to-backscatter ratio for aerosol, also

12   called lidar ratio (LR). For the January-May 2020 period, the values of LR derived with the

13   lidar, are 88 and 60 sr for altitude above and below 23 km respectively. These values are

14   obtained from the attenuation of the lidar signals by using the methodology described by Uchino

15   et al. (1983) and by Young (1995). The aerosol depolarization is computed from the backscatter

16   coefficient and the total linear volume depolarization ratio (Sakai et al., 2003). This latter is

17   obtained by taking the ratio of the perpendicular to total components of the backscattered signal

18   at 532 nm. To investigate the aerosol variability induced by the Australian fires, it is needed to

19   define a background profile. The background profile is built from measurements performed

20   when atmosphere is not undergoing major disturbance (e.g, volcanic eruptions, pyro-convection

21   outbreaks). In the present work, the background extinction profile at Lauder is built from

22   measurements performed between 1997 and 2004.

2.1.2 Reunion Island ground-based lidars

24   The Atmospheric Physics Observatory of La Réunion (OPAR) is a permanent station for long

25   term atmospheric observations (Baray et al., 2013). In particular, two lidar systems operating

26   in the UV (355 nm) and visible part of the light spectrum (532 nm) are used to retrieve ozone

27   and aerosols profiles at the Maïdo Observatory situated at 2200 m above mean sea level

28   (AMSL). These systems, named LiO3T (532 nm) and LiO3S (355 nm) are described by Duflot

29   et al. (2017) and by Baray et al. (2006), respectively. These lidars measure aerosol optical

30   properties (extinction, backscatter ratio) from ~15 km to the middle stratosphere, up to ~35 km,

31   with a high vertical resolution (15 m). Operating at two distinct wavelengths, the synergy of

32   Reunion lidar profiles allows us to assess the Angström exponent of aerosols between 355 nm

33   and 532 nm. In this study, the inversion process used the Klett method (Klett, 1985) with an

34   assumed lidar ratio of 60 sr, typical of aged BB aerosols (Müller et al., 2007). In the present

1 study we used 9 lidar profiles recorded during the January-March 2020 period. The background

2 extinction profile at Reunion is built from measurements performed between 2017 and 2019

3 excluding the perturbation induced by the Calbuco eruption in April 2015 (Bègue et al., 2017).

4 **2.1.3 CALIOP**

5 Cloud-Aerosol Lidar with Orthogonal Polarization (CALIOP) is a nadir pointing lidar orbiting

6 the Earth onboard the Cloud-Aerosol Lidar and Infrared Pathfinder Satellite Observation

7 (CALIPSO) satellite since 2006. CALIOP is a two-wavelength polarization-sensitive lidar (532

8 and 1064 nm) that measures total attenuated backscatter vertical profiles with altitude-varying

9 vertical (30–300 m) and horizontal (300–5000 m) resolution. In the present study, we used

10 CALIOP product version 3.3 level 1B which includes calibrated attenuated backscatter along

11 with collocated meteorological information provided by the National Aeronautics and Space

12 Administration Global Modeling and Assimilation Office (GMAO). These data are

13 postprocessed using a treatment described and validated by Vernier et al. (2009). The Scattering

14 Ratio (SR) profiles used for the detection of the smoke plume are calculated following the

15 methodology described by Khaykin et al. (2018). As a first step, the collocated GMAO data is

16 used to correct the backscatter profiles of molecular attenuation and ozone absorption. Then,

17 the SR is calculated as the ratio of total and molecular backscatter coefficients, with the latter

18 derived from GMAO air density. The SR profiles are recalibrated at 36-39 km, following the

19 methodology given by Vernier et al. (2009). The data with depolarization larger than 30 % are

20 discarded to the treatment in order to avoid aliasing cirrus clouds above the thermal tropopause.

21 The CALIOP data were obtained from the ACDISC data archive (ftp://acdisc.gsfc.nasa.gov)

22 hosted by NASA Goddard Space Flight Center.

23 **2.1.4 Sun photometry measurements: Sky radiometer**

24 A sky radiometer is a scanning sun-sky photometer able to perform measurements of direct sun

25 and diffuse sky irradiance under clear sky conditions, at seven wavelengths (between 315 and

26 1020 nm) and at several scattering angles. The direct solar extinction and diffuse sky radiance

27 measurements are used to derive the aerosol optical properties such as Aerosol Optical Depth

28 (AOD), Single Scattering Albedo (SSA) and aerosol size-distributions using the algorithm

29 developed by Nakajima et al. (1996). A detailed description of the sky radiometer and the

30 associated data retrieval is given by Hashimoto et al. (2012). In the present study, we used the

31 sky radiometer observations performed at Lauder in the framework of the SKYNET network.

32 SKYNET is a ground-based network of sky radiometers with observation sites spread over Asia

33 and other areas. Previous works have shown that the AOD from SKYNET is obtained with high

34 accuracy similar with that of the standard Langley method and with those from AERONET

1   (Campanelli et al., 2007; Che et al., 2008). At Lauder, the sky radiometer measurements have

2   been made since 2011. These observations are used in the present study to investigate the

3   aerosol variability induced by the passage of the Australian BB plume over Lauder. The

4   background evolution of AOD is built with measurements performed between 2011 and 2018.

5   The sky radiometer data used in this work are available on the SKYNET platform:

6   https://www.skynet-isdc.org/

7   **2.1.5 OMPS-LP**

8   The Ozone Mapper and Profiler Suite Limb profiler (OMPS-LP) has been flying on the Suomi

9   National Polar Partnership (NPP) satellite platform since October 2011. In the present study,

10 we use aerosol extinction profile from the NASA OMPS data product version 2.0 (Taha et al.,

11 2021). The aerosol extinction profiles are retrieved from the limb scattering solar radiation. The

12 V2.0 algorithm uses OMPS-LP measurements at wavelengths 510, 600, 675, 745, 869 and 997

13 nm, selected to minimize the effect of gaseous absorption (Taha et al., 2021). Aerosol extinction

14 measurements are provided from 10 to 40 km altitude on a 1 km vertical grid. A near-global

15 coverage is produced within 3-4 days. The OMPS data are used in the present study to

16 investigate the global transport of aerosol BB plume and its influence on the aerosol variability

17 over Reunion. As recommended by Taha et al. (2021), we use aerosol extinction measurements

18 at 745 nm. The background extinction profile is built with measurements performed from 2012

19 to 2014 and from 2016 to 2018. These periods are chosen in order to discard the perturbation

20 induced by the Calbuco eruption (Bègue et al., 2015). The OMPS data are downloaded from:

21 https://ozoneaq.gsfc.nasa.gov/.

22 The aerosol absorbing index (AAI) data from OMPS are also used to describe the transport of

23 the aerosol BB plume. This index allows the detection of absorbing aerosols through the

24 spectral difference between a given pair of UV wavelength. When its value is positive, it

25 indicates the presence of UV-absorbing aerosols such as dust and smoke. Conversely, a

26 negative value indicates the presence of non-absorbing aerosols while values close to zero are

27 found in the presence of clouds. The AAI data used in this work are available on the NASA

28 Earth Data platform: https://earthdata.nasa.gov/earth-observation-data

29 **2.2 CO and water vapor measurements**

30 **2.2.1 FTIR**

31 The total columns and volume mixing ratio profiles of trace gases such as CO are retrieved with

32 high accuracy and precision with ground-based Fourier Transform Infrared (FTIR)

33 spectrometers (Clerbaux et al., 2008; Vigouroux et al., 2015; Zhou et al., 2019). In the present

34 study, we use the FTIR observations performed at Lauder and Reunion sites in the framework

8

1   of the NDACC and Total Carbon Column Observing Network (TCCON) networks

2   respectively. A detailed description of the FTIR systems involved in both networks and the

3   associated data retrieval is given by de Mazière et al. (2018) and Wunch et al. (2015). A brief

4   description is given hereafter. The CO measurements from FTIR at Lauder have been made

5   since the early 1990s. The measurements are made using a Bruker high-resolution spectrometer

6   over a wide spectral range (around 600–4500 cm^{-1}). The CO dataset used in this study is the

7   same as that used by Bègue et al., (2021) and Kloss et al., (2019). Details on the spectral

8   measurements, CO retrieval strategy and derived CO column abundances can be found within

9   these references. The CO total columns and volume mixing ratio profiles on 48-layer

10   atmosphere (0.37–100 km asl) used in this study for the Lauder site are downloaded from the

11   NDACC website (http://www.ndacc.org).

12   The FTIR measurements at Reunion have been routinely performed in the framework of the

13   TCCON network since 2011. A Bruker high-resolution spectrometer over a wide spectral range

14   is also used at Reunion. The CO and O_2 total columns are simultaneously retrieved by using the

15   GGG2014 code (Wunch et al., 2015). Column-averaged dry-air mole fraction of CO are

16   obtained from the retrieval of these two components. TCCON uses the O_2 total to determine

17   the total column of the dry air. Then, the column-averaged dry-air mole fraction of CO is

18   calculated as the ratio between the retrieved CO total columns and the total columns of the dry

19   air. The abundance of CO used in the study for Reunion are downloaded from the TCCON

20   database   (http://www.ndaccdemo.org/about/cooperating-networks/total-carbon-column-

21   observing-network). In the present study, the background evolution of CO is built with

22   measurements performed between 2015 and 2018 (De Mazière et al., 2017).

23   **2.2.2 IASI**

24   The Infrared Atmospheric Sounding Interferometer (IASI) measures chemical species such as

25   CO by using a Fourier Transform spectrometer (Clerbaux et al., 2009; Coheur et al., 2009). It

26   is flying onboard the three Metop satellites. Retrieval of CO total and partial columns occurs in

27   near real-time from the nadir radiances measured by the instrument in the thermal infrared

28   radiation covering wavelengths from 6.62 to 15.5 µm. Global distributions are obtained for day

29   and night measurements, with a vertical range covering the troposphere and the lower

30   stratosphere. The total and partial column of CO are retrieved by using the Fast-Optimal

31   Retrievals on Layers for IASI (FORLI-CO, Hurtmans et al., 2012). Furthermore, the

32   contamination of the data by clouds is checked and flagged. In the present study, we used CO

33   columns from IASI instruments on Metop-A and Metop-B, which have been operating since

1   2006 and 2012, respectively. The IASI products used in this work are available on the AERIS

2   platform: https://iasi.aeris-data.fr/CO.

3   **2.2.3 MLS**

4   The Microwave Limb Sounder (MLS) performs vertical profile measurements of multiple trace

5   gases in the UT-LS onboard Aura satellite since 2004 (Waters et al., 2006). In the present study,

6   the CO and water vapor observations (version 5) from January 2017 to January 2020 over a

7   global domain extending between $10°$S and $25°$S in latitude and $30°$E and $60°$E in longitude have

8   been used. All MLS version 5 retrieval quality flags (quality, status, convergence, and

9   precision) were properly adhered to for all of our analyses (Livesey et al., 2020). Generally,

10   recommended pressure levels for science applications with CO and water vapor MLS data range

11   from 0.0215 to 215 hPa (http://mls.jpl.nasa.gov/ data/v4-2_data_quality_document.pdf). The

12   CO and water vapor profiles from MLS are obtained from the Atmospheric Composition Data

13   and Information Services Center (ACDISC) archive (ftp://acdisc.gsfc.nasa.gov) hosted by the

14   NASA Goddard Space Flight Center.

15   **2.3 Numerical Modelling**

16   **2.3.1 FLEXPART Model**

17   The Lagrangian transport and diffusion model FLEXPART version 10.4 is used to simulate

18   long-range transport of atmospheric tracers (Pisso et al., 2019; Stohl et al., 2005). This version

19   of FLEXPART includes improvements in different aspects such as physico-chemical

20   parameterizations (Pisso et al., 2019). Source identification occurs via the release of particles

21   from a receptor location and the simulation of backward trajectories. Model calculations are

22   based on ERA5 (Hersbach et al., 2020) meteorological data from the European Center for

23   Medium-Range Weather Forecasts (ECMWF) extracted at 3-hourly intervals with a horizontal

24   resolution of $0.5° \times 0.5°$ and a vertical resolution of 137 hybrid model levels (from the ground

25   to 0.01 hPa pressure altitude).

26   The model simulations are run with the aerosol (BC and OC) and CO tracers assuming removal

27   by dry and wet deposition for aerosols and OH reactions for CO. Each simulation consists of

28   20,000 particles released over Reunion during one day at altitudes between 15 and 19 km every

29   0.5 km and followed backward in time during one month. The simulation of backward

30   trajectories with FLEXPART for a long period (1-2 months) were previously explored in

31   previous studies (Aliaga et al., 2021; Eckhardt et al., 2017; Xu et al., 2021). The simulations

32   include the parameterization of turbulence and the activation of the convection. FLEXPART

33   model outputs are distributed over a regular vertical grid of 0.5°x 0.5° from ground to 25 km in

34   altitude. The model outputs are used to discuss the residence time of the BB aerosols and CO,

1   and their contributions on the variability of the aerosol optical properties and CO over the SWIO

2   basin. Discussions are based on the analysis of the emission sensitivity obtained from backward

3   simulations. The residence time of particles are integrated over the entire atmospheric column

4   and over the latitude to create averaged-map and longitudinal cross-section map and to provide

5   information on the geographical and vertical dispersion of BB aerosols in the atmosphere. The

6   BB contributions on the vertical distribution of CO and the aerosol optical properties can be

7   calculated by combining the potential emission sensitivity (PES) with an emission inventory.

8   PES represents FLEXPART particles only in the layer/altitude at which the emissions are

9   injected. Pyro-convection is not taking into account in the model (nor ECMWF data). Then, a

10   mass concentration profile of BB aerosol and CO is extracted by summing all the output grid-

11   points. A layer between 0 and 3 km is used for the BB in Africa (as observed in GFAS "top

12   altitude of plume", Kaiser et al., 2012) and between 9 and 16 km for the Australian fires (as

13   observed by CALIOP observations)

14   In the present study, the Global Fire Assimilation System (GFAS) version 1.2 emission (Kaiser

15   et al., 2012) has been used for the calculation. In addition, the Global Air Pollutant Emissions

16   - EDGAR v6.1 emission inventory (Kaiser et al., 2012, http://edgar.jrc.ec.europa.eu) is used for

17   CO for the year 2018 with a $0.1° \times 0.1°$ grid. These emissions represent the total CO emissions

18   by anthropogenic activities by excluding large scale BB with Savannah burning, forest fires.

19   As for the BB emissions, multiplying the CO emission flux from this inventory with the

20   FLEXPART emission sensitivity for a layer between 0 and 1 km gives access to the contribution

21   of anthropogenic sources to the total CO abundance. At the end of the process, in the case of

22   aerosols, the mass concentration profile is converted in extinction profile in order to discuss on

23   the contribution of BB aerosols on the vertical distribution of the aerosol extinction observed

24   from Lidar over Reunion. The conversion is performed by the use of Mie scattering model

25   assuming spherical particles with a density of 2 $g.cm^{-3}$ and a refractive index of 2.0 + 0.64i

26   adapted to optically absorbing aerosols.

27   ### 2.3.2 MIMOSA Model

28   The Modèle Isentropique de transport Mésoéchelle de l'Ozone Stratosphérique par Advection

29   (MIMOSA) model is a potential vorticity (PV) advection model running on isentropic surfaces

30   at a resolution of $0.3° \times 0.3°$ (Hauchecorne et al., 2002). The advection scheme is semi-

31   Lagrangian with a time step of 1 h and driven by ECMWF meteorological analyses. The model

32   can be run continuously in order to follow the evolution of PV filaments for several months.

33   The accuracy of the model has been evaluated by Hauchecorne et al. (2002) and validated

34   against airborne lidar ozone measurements using a correlation between PV and ozone, a quasi-

1 conserved chemical tracer on timescales of a week or so within most of the lower stratosphere

2 (Heese et al., 2001). The MIMOSA model can also be used to determine the origin of air masses

3 influencing a given site, similar to an isentropic Lagrangian trajectory model (Bencherif et al.,

4 2011; Hauchecorne et al., 2002; Portafaix et al., 2003; Bègue et al., 2017).

5 6 3. Transport of the Australian BB plume over the Southern Hemisphere

7 3.1 Formation of an intense stratospheric smoke layer

8 Following the strongest outbreak during New Year's Eve, a wide plume of BB aerosol with

9 large values of AAI (higher than 12) is transported toward the Tasman Sea on 1st January 2020

10 (Fig. 1a). Figure 1b depicts the CALIOP attenuated scattering ratio (SR) profiles on 1st January

11 2020 above New-Zealand. The CALIOP attenuated SR profiles are calculated along the

12 CALIOP track (blue line in Fig. 1a) crossing the absorbing aerosol plume. CALIOP

13 observations reveal a broad region of high values (ranging from 10 to 25) between 36° S and

14 46°S centered at 16.5 km altitude (Fig. 1b). Khaykin et al. (2018) reported similar values during

15 the passage of the 2017 Canadian smoke plume over Observatoire de Haute-Provence (OHP,

16 France). Figure 1 reveals that New Zealand was significantly exposed to the transport of the

17 Australian BB plume. The ground-based measurements recorded in New-Zealand are helpful

18 to investigate the evolution of the aerosol smoke. Figure 2a illustrates the daily extinction

19 profiles at 532 nm derived from lidar measurements over Lauder between 1st December 2019

20 and 1st April 2020. Note that a strong convective activity prevented lidar operations between

21 mid-December 2019 and the 1st January 2020. Figure 2a reveals a sharp increase in the

22 extinction in the stratosphere over Lauder starting from mid-January 2020 with values ranging

23 from 3×10^{-3} km^{-1} to 9×10^{-3} km^{-1}, one order of magnitude above the typical stratospheric

24 aerosol background (Vernier et al., 2012). The vertical extent of the plume increased

25 significantly between mid-January and 1st April 2020 with an aerosol layer spanning from 11.5

26 to 20 km. The ascent of the aerosol plume could be attributed to efficient adiabatic heating as a

27 result of the strong absorption of solar radiation by this black carbon rich plume. This is

28 consistent with the results found by De Laat et al. (2012) during the Australian Black Saturday

29 fires occurring on February 2009. They showed a strong ascent of the BB aerosol due to

30 adiabatic heating effect. Figure 2b depicts the daily evolution of CO mixing ratio profile

31 obtained from FTIR measurements over Lauder between 1st December 2019 and 1st April 2020.

32 Prior to the convective period, the maximum of CO mixing ratio (120-130 ppbv) is observed in

33 the troposphere. An increase of CO mixing ratio in the lower stratosphere is visible from mid-

1   December 2019. One can observe that the maximum of the CO mixing ratio (50-90 ppbv) is

2   mainly observed in the UT-LS (9-13 km) during the February-April 2020 period.

3   The injection of BB aerosols and CO in the stratosphere induced significant disturbance evident

4   in the total columns over Lauder (Fig. 3a). Figure 3a depicts the monthly mean evolution of

5   AOD and total columns of CO (TCO) at Lauder between 1st December 2019 and 1st April 2020

6   obtained from sky-radiometer and FTIR measurements respectively. AOD reaches its

7   maximum value (0.17, 3 times higher than background value) in January 2020, decreasing to

8   background values in February 2020 (Fig. 3a). The similar evolution is also observed for the

9   TCO values. An abrupt increase in TCO (~9 % of the pre-event levels) is observed in January

10   2020 and the return to pre-event values is observed as of February 2020 as also already shown

11   in Kloss et al. (2021). Conversely, the perturbation on the stratospheric columns still persisting

12   after February 2020. Figure 3b illustrates the monthly mean evolution of stratospheric AOD

13   (sAOD) and CO columns (sCO) at Lauder between 1st December 2019 and 1st April 2020. The

14   sAOD and sCO are calculated between 12 and 30 km from lidar and FTIR measurements,

15   respectively. Figure 3b indicates that the evolution of sAOD and sCO is fairly similar. A

16   statistically significant increase of sAOD is observed in January 2020 (2.5 times higher than

17   background value) and still visible in April 2020 with same amplitude. sCO reaches its

18   maximum values (~24 % of the pre-event levels) in January 2020 and slightly decreases in April

19   2020 (~14% of the pre-event). This result is consistent with results found by Khaykin et al.

20   (2020). Based on the MLS observations, Khaykin et al. (2020) showed that the stratospheric

21   mass of CO within the southern extra-tropics increased abruptly by around 20% compared to

22   the observed value during the pre-event period.

23   Our results agree with previous studies (Kablick et al., 2020; Khaykin et al., 2020, Kloss et al.,

24   2021) and confirm a persistent perturbation on the atmospheric composition of the extra-

25   tropical stratosphere. In order to extend the discussion, the spatial dispersion of the smoke layer

26   will be discussed in the next section.

27   **3.2 Spatial dispersion of sAOD and CO**

28   Figure 4 depicts a time-averaged map of partial columns of aerosols (between 16 and 30 km,

29   sAOD) and CO (between 9 and 30 km) obtained from OMPS and IASI observations between

30   9th and 16th January 2020, respectively. One can observe the correlation in the shape and spatio-

31   temporal distribution between CO and sAOD over the Southern Pacific (Figs 4a and 4b). It is

32   worthwhile mentioning that the transport of the aerosol (with values ranging from 6×10^{-3} to 1

33   $\times 10^{-2}$ km^{-1}) and CO (with values ranging from 6 to 8×10^{17} molecules. cm^{-2}) plume over the

34   Southern Pacific occurred mainly within the 18°S–60°S latitudinal band. The plume's structure

1 over the Southern Pacific can be explained by the fact that the core plume started to encapsulate

2 into a compact bubble-like structure (with 4 km vertically extended and 1000 km horizontally

3 wide) on 7th January 2020 (Khaykin et al., 2020). Figures 4a and 4b reveals that the aerosol and

4 CO plume cross the Southern Pacific fairly quickly. Based on CALIOP and Lidar observations

5 at Punta Arenas (53.2°S, 70.9°E, Chile), Ohneiser et al. (2020) showed that aerosols injected

6 into the lower stratosphere over southeastern Australia crossed the Pacific Ocean within 10

7 days. On 10th January 2020, the aerosol plume is already visible over Punta Arenas and

8 structured into two layers. One can observe an aerosol band (with values ranging from 5×10^{-3}

9 to 9×10^{-3} km^{-1}) across the Southern Hemisphere between 40°S and 60°S during the 9-16th

10 January 2020 period (Figure 4a). Therefore, the Australian aerosol plume has already circled

11 the Southern Hemisphere during the first two weeks of January 2020. Based on MLS and

12 CALIOP observations, Khaykin et al. (2020) showed that the smoke layer dispersed across the

13 whole Southern Hemisphere extra-tropics in less than two weeks whereas the carbon-rich core

14 remained bounded within the mid-latitudes (30°S-50°S). The fastest patches of smoke returned

15 over Australia by 13th January 2020 (Khaykin et al., 2020). The same conclusion cannot be

16 made for CO from space-borne observations (Figure 4b). One can observe weak values of CO

17 (less than 5×10^{17} molecule.cm^{-2}) over southern Atlantic and without real link with the large

18 plume observed over southern Pacific (Fig. 4b). Except for the bubble structure, it seems that

19 the main part of the Australian BB plume has been transported bounded within the extra-tropical

20 latitudinal band. Further discussions the dispersion of the Australian smoke layer over the

21 SWIO basin will be given in the next section.

4. Presence of aerosols smoke layer over the SWIO basin

4.1 Aerosol and CO variability over a subtropical site: Reunion

24 Figure 5a depicts the evolution of the sAOD at 532 nm calculated between 15 and 30 km from

25 the ground-based lidars (LiO3T and LiO3S) and OMPS observations over Reunion from 1st

26 January to 1st March 2020. The Angström exponent for the 532–745 nm wavelength pair is

27 adopted from methodology in Taha et al. (2021) and set to 1.9. lidar observations over Reunion

28 are also used to calculate the aerosol Angstrom exponent (using 355 nm and 532 nm pairs). An

29 abrupt increase in the aerosol loading is clearly observed over Reunion as of 16th January 2020

30 according to satellite observations. This increase of the aerosol loading, three times above the

31 typical background, was still visible until 1st March 2020. It is worthwhile mentioning that the

32 sAOD values observed between 16th January and 1st March 2020 are higher than those observed

33 during the passage of the Calbuco plume over Reunion site, which did not exceed 0.013 (Bègue

34 et al., 2017). The increase of sAOD in mid-January coincided with an increase of CO, as shown

1   in Figure 5b based on the use of total columns and CO abundance from IASI and FTIR at the

2   same site and over the same period. The evolution of CO obtained from IASI and FTIR

3   measurements correlate. The ground-based and satellite observations clearly indicate a

4   significant increase of CO with a peak observed in mid-January. The ground-based observations

5   show that the CO abundance observed during this increased phase is on average 20% higher

6   than the values observed during the background period (Fig. 5b). The evolution of sAOD and

7   CO observations in mid-January suggests that Reunion, and its surrounding, have been

8   influenced by the transport of smoke aerosol layers.

9   Figures 6a and 6b illustrate the night-averaged extinction profiles at 355 nm derived from lidar

10   measurements over Reunion on January and February 2020, respectively. The two first weeks

11   of January 2020 are representative of the January typical background (shaded area), as

12   illustrated on 13th January 2020 (Fig. 6a). Conversely, the extinction profiles at the end of

13   January 2020 (27th and 28th) are marked by a significant increase (4 times higher than the

14   background values) located in the lower stratosphere between 16.8 and 18 km altitude

15   (equivalent to potential temperature levels 380-404 K). One can observe that the structure of

16   the extinction profile in the lower stratosphere has changed between these two days. On 28th

17   January, the extinction profile exhibits a sudden increase at 17.4 km (~400 K) and quickly

18   decreased afterwards to values observed the previous day (Fig. 6a). It is worthwhile mentioning

19   that the values of extinction (10 to 17×10^{-3} km^{-1}) observed in the lower stratosphere on these

20   two days are of the same order as those observed at Lauder a few days after the pyro-convective

21   event (Fig. 2). Figure 6a reveals a statistically significant increase (4 times higher than

22   background values) in aerosol extinction between 15 and 16.5 km altitude (361-375 K), on 27th

23   and 28th January 2020. Over Reunion, the lidar observations hence confirm the presence of a

24   significant aerosol layer in the UT-LS by the end of January. In February, the extinction profiles

25   clearly exhibit two significant aerosol layers with the first one located between 16 and 19.5 km

26   (370-440 K) and the second one between 20 and 22.5 km (465-500 K) (Fig. 6b).

27   To further discuss the optical properties of these aerosol layers, the Angstrom exponent has

28   been calculated between 355 nm and 532 nm from the LiO3S and LiO3T measurements (Figs.

29   6c and 6d). In February, the Angström exponent values reveal that the two aerosol layers consist

30   mainly of small aerosol particles (Fig. 6d), consistent with a stratospheric smoke layer (Haarig

31   et al., 2018; Hu et al., 2019; Ohneiser et al., 2021). In January, the profile of Angström exponent

32   exhibits more variability in the UT-LS (Fig. 6c) with values ranging from 0.6 to 1.9, on 27th

33   and 28th January. Based on the literature, the largest proportion of the observed Angström

34   exponent range (up to ~1.5) within the plume, points to the presence of an aerosol smoke layer

1   (Das et al., 2021; Haarig et al., 2018; Hu et al., 2019; Kloss et al., 2019). The wide range of

2   Angström exponent values suggests that the aerosol layer is not homogeneously distributed at

3   this stage and might be interpreted as a mixture of fresh and aged smoke layers (Fig. 6c). This

4   may indicate growth and removal processes (e.g., coagulation, condensation, sedimentation)

5   which can modulate the morphology and mixing state of the aerosol layer during its transport

6   (Burton et al., 2015; Hamil et al., 1997). The residence time of the aerosol particles in the

7   atmosphere depends on the balance between the growth processes and the removal processes,

8   which are likely to be controlled by the dynamical context. Previous works showed that the

9   dynamical context can modulate the structure and optical properties of the aerosol layer over a

10   given site from day to day (Bègue et al., 2017; Kremser et al., 2016). Fresh aerosols can be

11   rapidly transported and mixed with pre-existing aged aerosol. Given the fact that the Angström

12   exponent values decrease with the duration of transport, we cannot exclude that the vertical

13   distribution of optical properties of aerosol over Reunion may also be explained by the regional

14   transport of air masses.

15   **4.2 Origin of the air masses**

16   To analyze the origin of air masses at Reunion on 27th and 28th January, one-month backward

17   trajectories are calculated using FLEXPART (Aliaga et al., 2021; Eckhardt et al., 2017; Xu et

18   al., 2021). A period of one month is chosen because it refers to time separating the pyro-

19   convective outbreak event and the day of the measurement at Reunion. The representation of

20   the PES (potential emission sensitivity) from back-trajectories simulations initialized at 18 km

21   originating from Reunion on 27th and 28th January 2020 are presented in Figure 7.

22   Figures 7A-1 and 7B-1 display the horizontal trajectory paths, whilst vertical movement is

23   shown in Figures 7A-2 and 7B-2, respectively. The vertical transect of FLEXPART back

24   trajectories in Figure 7A-2 confirms a high probability of air mass contribution from the

25   Australia if the fires emissions are directly injected into the stratosphere by convection (black

26   rectangle in the figure), (i.e. layer of 9 to 16 km of injection taken for the PES, see section

27   2.3.1). Then, according to FLEXPART results, the air masses at 18 km over Australia moved

28   westward and reached Reunion on 27th January. One can observe that the same pattern is

29   observed on 28th January 2020 (Figs. 7B-1 and 7B-2). One part of the Australian smoke layer

30   is advected zonally by the prevailing easterly winds and is observed over Reunion on 27th and

31   28th January 2020 at 18 km. It is worthwhile mentioning that the same pattern has been observed

32   during the volcanic eruption of the Hunga Tonga on January 2022 (Baron et al, 2023, Kloss et

33   al., 2022; Sellitto et al., 2022). The FLEXPART simulations also suggest that Reunion is also

34   influenced by eastward transport of air masses. This pathway is clearly visible on 28th January

1   2020 (Figs. 7B-1 and 7B-2). Figure 7B-1 reveals that air masses coming from the South

2   American region and Australia region both reach the SWIO basin by passing over southern

3   Africa. Furthermore, air masses from high latitudes seem to cross the subtropical latitudes

4   following a wave shape and reach the SWIO basin by passing over the Cape of Good Hope

5   (Figure 7B-1).

6   In order to improve the discussion on this eastward transport of air masses over the SWIO basin,

7   the MIMOSA model has been used to produce a continuous evolution of PV fields for the period

8   from 1st to 31st January 2020. Two advected PV maps derived for the 400 K isentropic level

9   from the MIMOSA model are depicted in Figure 8. The localization of the aerosol plume

10   obtained from OMPS observations at the 400 K ± 5 K isentropic level are also superimposed

11   (Fig. 8). The 400 K isentropic level is chosen according to the layers observed in the extinction

12   profiles over Reunion between 390 and 404 K isentropic level on 27th and 28th January 2020

13   (Fig. 6a). Figure 8 reveals significant wave activity during these two days. It is clearly shown

14   that air masses from mid-latitudes (40-60°S) cross the subtropical latitudes (20-40°S) and are

15   advected eastward between South Africa and Madagascar following a wave shape. Given the

16   Australian BB aerosol are mainly located in the mid-latitudes (Fig. 4a), we can reasonably

17   conclude that the filament reaching the SWIO basin contains aerosol from Australian BB event.

18   On 27th January, air masses containing aerosol are observed at Madagascar and its surroundings

19   (Fig. 8a). These air masses are advected eastward following the displacement of the wave shape

20   and reach Reunion, on 28th January (Fig. 8b). These results demonstrate that the unusual aerosol

21   load observed in the UT-LS above SWIO is to be linked to the Australian fires. Parts of the

22   smoke plume underwent an isentropic transport from the mid to tropical latitudes following two

23   distinct pathways to reach Reunion.

24   Nevertheless, the contribution of the Australian BB event on the variability of aerosols in the

25   upper troposphere (15-16.5 km; 361-375 K) remains ambiguous. The representation of the PES

26   from back-trajectories simulations initialized at 16 km originating from Reunion for the 27th

27   and 28th January 2020 are presented in Figure 9. Figure 9A-1 and 9B-1 reveal that the

28   trajectories from Reunion at 16 km pass over southern Africa and Madagascar. One can observe

29   that the highest values of PES are located over southern Africa and Madagascar (Figs. 9A-1

30   and 9B-1). Furthermore, the FLEXPART simulations suggest that air masses from southern

31   Africa and Madagascar might have reached altitudes up to 16 km between 25°E and 55°E in

32   longitude and reached Reunion on 27th and 28th January 2020 (Figs. 9A-2 and 9A-2). The results

33   of Figure 9 show an influence of air masses coming from Africa and reaching the SWIO basin

34   at 16 km. Thus, the moderate increase in aerosol extinction observed in the upper troposphere

1   (between 16 and 17 km altitude) on 27th and 28th January in Figure 6a may be attributed to air

2   masses from regional sources, namely southern Africa and Madagascar.

3   In summary, our analysis suggests that the variability of CO and aerosols in the UT-LS over

4   the SWIO basin in January is explained both by long-range and regional transport of air masses.

5   The extent to which regional sources have contributed to the variability of the atmospheric

6   compounds over the SWIO is now investigated.

7   5. Discussion on the influence of the regional sources

8   We investigate the contribution of the African and Australian BB activity on the atmospheric

9   composition in the UT-LS over the SWIO basin. Because a significant simultaneous increase

10 of CO and sAOD is observed over Reunion and its surroundings from 16th to 29th January 2020,

11 the discussion will focus on this period. In order to assess the contribution of African and

12 Australian BB activity, FLEXPART is coupled with the GFAS inventory.

13   5.1 Presence of African air masses in the UT-LS

14 The location of fire-flagged pixels and the associated Fire Radiation Power (FRP) values from

15 MODIS between 16th and 29th January 2020 are reported in Figure 10a. FRP gives quantitative

16 information on combustion rates and its intensity. The sparse activity of the African fires in

17 January is clearly illustrated in Figure 10a with moderate values of FRP ranging from 20 to 200

18 MW.m^{-2}. These values are ten times lower than those observed over the southeastern Australia

19 between 30th December 2019 and 12th January 2020 (Bègue et al., 2021). One can observe that

20 the African BB activity in January 2020 is mainly located over the northwestern (near the

21 Equator) and southeastern side of southern Africa. The most intense values (100-200 MW.m^{-2})

22 are observed over the southeastern side.

23 Despite this sparse activity of BB, the amount of CO injected into the atmosphere is fairly

24 significant and ranging from 5 to 6×10^{17} molecules.cm^{-2}. Time-averaged map of the partial

25 column of CO (between 9 and 30 km) from IASI observations between 16th and 29th January

26 2020 over the SWIO basin is reported on Figure 10b. The partial column of CO over the

27 southern Africa is characterized by two regions of high values (higher than 5×10^{17}

28 molecules.cm^{-2}). The first region stretches between the eastern side of southern Africa and

29 western side of Madagascar which corresponds to a domain extending between $10°S$ and $25°S$

30 in latitude and $30°E$ and $45°E$ in longitude (Fig. 10b). The second region is located on the

31 opposite side, over a domain extending between $10°S$ and $15°S$ in latitude and $5°E$ and $15°E$ in

32 longitude. These regions of high values of CO seem to be mainly related to BB activities located

33 over the northwestern side of southern Africa (Fig. 10a). Although these BB activities are less

34 intense than those observed over the southeastern side, they seem to have the potential to impact

1   the variability of CO between 9 and 30 km over the SWIO basin. This could be explained by

2   convective activity which can rapidly transport air masses from the boundary layer to the upper

3   troposphere (Pfister et al., 2010; Blamey and Reason, 2012). Previous works showed that,

4   during the southern summer, the convective activity over southern Africa and the SWIO basin

5   is triggered either from the ITCZ or tropical storms (Barimala et al., 2018; Héron et al., 2020;

6   Lashkari et al., 2017).

7   Figure 10c depicts a time-averaged map of OLR (Outgoing Longwave Radiation) anomalies

8   from NCEP analysis between 16th and 29th January 2020. One can observe that the main

9   convective regions (region of negative OLR anomalies) are located in mainland Africa between

10   $12°$ S and $25°$ S and the northern side of the SWIO basin. It is worthwhile mentioning that the

11   daily brightness temperature values obtained from MODIS between 16th and 29th January 2020

12   (not shown) are ranging from 195 to 210 K over the eastern side of southern Africa and the

13   Mozambique Channel (around the north tip of Madagascar). These values of brightness

14   temperature can be attributed to deep convection clouds (Héron et al., 2020; Young et al., 2013).

15   In most tropical basins, the deep convection can be separated into local convection and tropical

16   storms (Bovalo et al., 2012). In our case, the deep convection activity could be explained by

17   the ITCZ activity moving southward, near the subtropical latitudes, during the austral summer

18   (Barimala et al., 2018; Lashkari et al., 2017). Through the analysis of ERA-Interim data over a

19   period of 66 years, Lashkari et al. (2017) investigated the annual and seasonal displacement of

20   the ITCZ. On average, the motion of ITCZ over southern Africa on January is characterized by

21   southward move from $5°$N to $20°$S in latitude occurring between $20°$ E and $35°$ E in longitude

22   (Lashkari et al., 2017). Over the Mozambique Channel, the deep convection can be explained

23   by the tropical storm activity. Indeed, a tropical depression has been formed in the east side of

24   the Mozambique Channel (near the northwestern side of Madagascar) between 20th and 22nd

25   January 2020. This tropical depression reached the stage of strong tropical storm on 24th January

26   2020 and was called Diane by the RMSC (Regional Specialized Meteorological Center) of

27   Reunion. The intensification of the tropical depression into strong tropical storm occurred

28   around the north tip of Madagascar. Diane passed near Reunion on 25th January 2020 (Fig. 10c).

29   In the present study, the convective activity over southern Africa and the SWIO basin may

30   hence be due to both ITCZ proximity and Diane activity. This convective activity also explains

31   the gap of CO observations from satellites over Madagascar and the northern side of southern

32   Africa (Fig. 10b).

33   To further discuss the vertical distribution of CO in the UT-LS within the region of deep

34   convection, the vertical cross section of CO and water vapor mixing ratio anomalies calculated

19

1   from MLS observations between 16th to 29th January 2020 are analyzed (Figs. 11a and 11b).

2   The CO and water vapor mixing ratio anomalies are calculated as a relative difference by

3   considering the monthly background means as the reference values. The calculations are

4   performed over a domain extending between $10°S$ and $25°S$ in latitude and $30°E$ and $60°E$ in

5   longitude (black box in Fig. 10b). The altitude-longitude cross-section is averaged for all

6   latitudes covering the study domain. This domain includes both the region of deep convection

7   and the first region of high values of CO. The monthly background is calculated from available

8   MLS observations between 2017 and 2019. The altitude-longitude cross-section is averaged for

9   all latitudes covering the study domain. Figure 11a exhibits two regions of high values of CO

10 mixing ratio anomalies (higher than 15%) centered at $37°E$ and $50°E$ in longitude. The

11 maximum CO mixing ratio anomalies in the first region are centered at 215 hPa (~12 km) with

12 anomalies ranging from 25% to 30%. The values of the anomalies decreased rapidly with

13 altitude. Indeed, the anomalies values obtained at 146 hPa (~15 km) and 100 hPa (~17 km)

14 ranged from 20% to 25% and from 15% to % respectively. In the second region, the maximum

15 CO mixing ratio anomalies are also centered in the middle troposphere (215 hPa). One can

16 observe that these regions of CO mixing ratio anomalies are in coincidence with two regions of

17 high values (higher than 20%) of water vapor mixing anomalies (Fig. 11b). The maxima of

18 water vapor mixing ratio anomalies are centered at 146 hPa with values ranging from 40% to

19 50%. This coincidence suggests a significant perturbation of the vertical distribution of CO and

20 water vapor mixing ratio induced by the convective activity over southern Africa and the SWIO

21 basin. Given the localization of the Diane tropical storm over the SWIO basin, we can

22 reasonably assume that it contributed significantly to impact the vertical distribution of CO and

23 water vapor in the second region aforementioned. One can observe that fire flagged pixels (with

24 FRP values range between 10 and 30 MW.m^{-2}) are detected by MODIS over the East of

25 Madagascar (Fig. 10a). We can assume that the convective activity induced by Diane near

26 Madagascar may have contributed to lift air masses enriched in CO from the lower troposphere.

27 This could explain the high values of CO mixing ratio anomalies observed in the second region.

28 This is consistent with the FLEXPART simulations which highlight a lift of air masses from

29 the lower troposphere to lower stratosphere between $25°E$ to $55°E$ in longitude (Figure 9). One

30 can observe that the most significant anomalies of the vertical distribution of CO and water

31 vapor mixing ratio stretch from the middle troposphere (215 hPa) up to the tropopause layer

32 (100 hPa,). The values observed in the lower stratosphere are less than those observed in the

33 troposphere. Indeed, the CO and water vapor mixing ratio anomalies at 68 hPa (~19 km) are

34 less than 10 % and 20 % respectively. At 68 hPa, it can be observed that high values of water

1   vapor mixing ratio anomalies are not in coincidence with high values of CO mixing ratio

2   anomalies, but located along the vertical extent of the maxima of CO mixing ratio anomalies in

3   the troposphere.

4   Our analysis corroborates the results found by Héron et al. (2020). Based on radiosonde and

5   satellite observations, Héron et al. (2020) showed that convective activity over the SWIO basin

6   has the potential to influence the variability of ozone and water vapor in the upper-troposphere

7   during the austral summer. In the present study, the satellite observations and FLEXPART

8   simulations strongly suggests that African air masses enriched in CO and aerosols were lifted

9   from the lower troposphere to the lower stratosphere due to convective activity. Our results

10 demonstrate that the variability of CO and aerosol over the SWIO basin can be explained both

11 by the influence of long-range transport of the Australian fires plumes, together with regional

12 transport from southern Africa, enhanced by convective activity due to the passage of a tropical

13 storm.

14   **5.2 Discussion on the variability of the total and partial column of CO**

15 The African and Australian BB contributions to CO measured concentrations over Reunion are

16 assessed by coupling the FLEXPART model with gases emissions from the GFAS inventory.

17 The emission sensitivity from FLEXPART, only at the altitude where the emissions are injected

18 (0-3 km for Africa fires and 9-16 km for Australian fires), is combined with CO emission

19 inventory. The CO emissions due to anthropogenic activity are also taken considered by

20 coupling the FLEXPART model with the EDGAR inventory. The evolutions of the total and

21 partial column of CO observed by IASI and simulated by FLEXPART from 15th to 29th January

22 over Reunion are depicted in Figure 12.

23 Despite the underestimation of the simulated total and partial column of CO, their overall

24 temporal evolution is fairly well reproduced by FLEXPART (Fig. 12). The discrepancies

25 between FLEXPART and IASI may be attributable to several possible caveats. A possible

26 source of error can be due to the fact that the vertical motion induced by pyro-convection is not

27 included in FLEXPART. We address this issue by applying an injection height in agreement

28 with CALIOP observations (9-16 km, Fig. 1) for the Australian plume (Khaykin et al., 2020).

29 An injection height ranging up to 3 km was chosen for the African fires (Labonne et al., 2007).

30 The injection height of the plume plays a key role in its long-range transport (Sofiev et al.,

31 2012). An inappropriate or unrealistic injection height can lead to either a dilution or an

32 overestimation of the plume. The injection height depends on the intensity of the fire, as well

33 as on the meteorological conditions. Another possible explanation in these differences can come

34 from the duration of the backward calculation (1 month) (Brocchi et al., 2018). Underestimation

1   of the total and partial columns of CO may also be the result of an underestimation of the CO

2   emissions by GFAS. In the framework of their FLEXPART simulation, Brocchi et al. (2018)

3   reveal that an amplification factor of 2 has been applied to CO emissions from GFAS to get

4   similar CO quantities to observations. Nevertheless, these simulations can reasonably be used

5   to discuss the contribution of CO emissions from Africa and Australia on the variability of the

6   total and partial columns of CO over the SWIO basin.

7   The contribution of the CO emissions from Africa and Australia on the total and partial columns

8   of CO over Reunion is isolated and depicted in Figure 12. On average, the CO emissions from

9   Africa contribute up to 90% of the enhancement of the total and partial column of CO from 15th

10 to 29th January. The transport of the CO plume induced by the Australian sources have not been

11 efficient over the SWIO basin. This could be explained by the fact that CO decays quickly due

12 to photochemical oxidation whose efficiency increase with altitude. Khaykin et al. (2020)

13 showed that the decay of CO within the bubble occurred during its transport over the Southern

14 Pacific on its way to the Indian ocean. The variability of CO over the SWIO basin is hence

15 mainly explained by the regional transport of air masses.

16   **5.3 Discussion on the variability of the aerosols**

17 The FLEXPART simulations for the contribution of aerosol (BC and OC) emissions from

18 Africa and Australia on the sAOD over Reunion use the same parameters as for CO, in

19 particular the injection height. The emission sensitivity from FLEXPART is combined with BC

20 and OC from the GFAS emission inventory. Figure 13 depicts the evolution of the sAOD

21 observed by OMPS and simulated by FLEXPART from 15th to 29th January over Reunion.

22 Unfortunately, few data have been recorded during the period aforementioned. Nevertheless,

23 the simulated sAOD compare fairly well with the available OMPS observations during this

24 period, and the sAOD peak observed on 19th January is acceptably well reproduced. Figure 13

25 reveals that the variability of the sAOD between 15 and 30 km altitude is mainly driven by the

26 aerosol emissions from Australia. On average, the aerosol emissions from Australia contributed

27 up to 95 % of the sAOD variability over Reunion from 15th to 29th January. One can observe

28 that the evolution of sAOD is not correlated to the evolution of the aerosol emission from Africa

29 which is marked by an increase from 21th to 29th January. The weak contribution of African

30 component on the sAOD can be explained by the fact that the amounts of African BB aerosols

31 injected in the atmosphere by the convective activity decrease with altitude. Moreover, it is

32 likely that aerosol would be scavenged by cloud droplets (taken into account in FLEXPART)

33 in a strongly convective environment such as tropical storm Diane. Overall, FLEXPART

34 simulations clearly suggested the contribution of African and Australian BB aerosols.

6. Summary and Conclusion

The complex aerosol and CO variabilities over the SWIO basin during the 2020 austral summer have been investigated. The meteorological context and the extensive fires over southeastern Australia were favorable to trigger pyro-convective events between 29th December 2019 and 12th January 2020. These pyro-convective events led to massive injection of combustion products in the stratosphere. The ground-based and space-borne lidars revealed the presence of an intense stratospheric smoke layer over the southeastern Australia region. Over the Lauder site in New Zealand, this smoke layer was detected in the stratosphere (centered at 16 km) until April and beyond. The analysis of the spatial and temporal dispersion of the Australian smoke layer highlighted its quick transport circling the entire Southern Hemisphere in less than two weeks. Furthermore, the satellite observations revealed that the transport of the Australian smoke layer has been mainly bounded within an extra-tropical latitudinal band.

Nevertheless, the numerical models clearly showed the influence of the Australian smoke layer on the variability of aerosol over the SWIO basin. Over Reunion, the aerosol extinction profiles exhibited a significant increase in the lower stratosphere during the end of January. The MIMOSA simulations highlighted the isentropic transport of the Australian BB aerosols from extra-tropical latitudes to Reunion at 400 K isentropic level, on 28th January. As a consequence, the corresponding aerosol extinction profile exhibited a sudden increase by drawing a structure similar to a laminae at the 400 K isentropic level. The aerosol extinction profiles also exhibited a moderate increase in the upper troposphere.

This paper investigates for the first time the possibility of the African emissions from BB to influence the CO and aerosol distribution in the UT-LS during the convective season. Despite the fact that African BB activity is usually sparse in January, it contributed to modulate the vertical distribution of CO and aerosols in the upper troposphere over the SWIO basin. The analysis of satellite observations and FLEXPART simulations suggested that because of the convective activity, air masses enriched in CO and aerosols have been lifted from the lower troposphere to the lower stratosphere. Air masses from Africa contributed up to 90% of the total and partial column (between 9 and 30 km) of CO variability over Reunion and its surroundings. The simulations shows that the modulation of the aerosol extinction in the upper troposphere and the lower stratosphere, over Reunion, was driven by the transport of air masses from both Africa and Australia, respectively. Our findings suggest simultaneous presence of African and Australian aerosol smoke layers at Reunion.

Data availability

The data used for this study are available and open access by request to scientist mentioned or through the link hereafter: Lidar measurements (tetsu@mri-jma.go.jp, nelson.begue@univ-reunion.fr), radiometer measurements (ben.liley@niwa.co.nz), FTIR measurements from TCCON network (mahesh.sha@aeronomie.be); Lauder FTIR data available on the NDACC public access database (https://www-air.larc.nasa.gov/missions/ndacc/data.html); The satellite observations and emission inventory used are available on-line from the sources as stated in the manuscript.

1 **REFRENCES**

2 Baray, J.-L., Courcoux, Y., Keckhut, P., Portafaix, T., Tulet, P., Cammas, J.-P., Hauchecorne,

3 A., Godin Beekmann, S., De Mazière, M., Hermans, C., Desmet, F., Sellegri, K., Colomb, A.,

4 Ramonet, M., Sciare, J., Vuillemin, C., Hoareau, C., Dionisi, D., Duflot, V., Vérèmes, H.,

5 Porteneuve, J., Gabarrot, F., Gaudo, T., Metzger, J.-M., Payen, G., Leclair de Bellevue, J.,

6 Barthe, C., Posny, F., Ricaud, P., Abchiche, A., and Delmas, R.: Maïdo observatory: a new

7 high-altitude station facility at Reunion Island (21° S, 55° E) for long-term atmospheric remote

8 sensing   and   in   situ   measurements,   Atmos.   Meas.   Tech.,   6,   2865–2877,

9 https://doi.org/10.5194/amt-6-2865-2013, 2013

10 Baray, J.-L., Leveau, J., Baldy, S., Jouzel, J., Keckhut, P., Bergametti, G., Ancellet, G.,

11 Bencherif, H., Cadet, B., Carleer, M., David, C., De Mazière, M., Faduilhe, D., Godin-

12 Beekmann, S., Goloub, P., Goutail, F., Metzger, J.-M., Morel, B., Pommereau, J.-P.,

13 Porteneuve, J., Portafaix, T., Posny, F., ROBERT, L., and Van Roozendael, M.: An

14 instrumented station for the survey of ozone and climate change in the southern tropics, 8,

15 1020–1028, https://doi.org/10.1039/b607762e, 2006.

16 Baron, A., Chazette, P., Khaykin, S., Payen, G., Marquestaut, N., Bègue, N. and Duflot, V.

17 (2023). Early Evolution of the Stratospheric Aerosol Plume Following the 2022 Hunga Tonga-

18 Hunga Ha'apai Eruption: Lidar Observations From Reunion (21° S, 55° E). *Geophysical*

19 *Research Letters*, *50*(10), https://doi.org/10.1029/2022GL101751, e2022GL101751.

20 Barthe, C., Bousquet, O., Bielli, S., Tulet, P., Pianezze, J., Claeys, M. and Zucule, J.: Impact of

21 tropical cyclones on inhabited areas of the swio basin at present and future horizons. part 2:

22 Modeling component of the research program renovrisk-cyclone. *Atmosphere*, *12*(6), 689, 2021

23 Bègue, N., Bencherif, H., Jegou, F., Vérèmes, H., Khaykin, S., Krysztofiak, G., Portafaix, T.,

24 Duflot, V., Baron, A., Berthet, G., Kloss, C., Payen, G., Keckhut, P., Coheur, P-F., Clerbeaux,

25 C., Smale, D., Robinson, J., Querel, R and Smale, P. : Transport and variability of tropospheric

26 ozone over Oceania and southern pacific during the 2019–20 Australian bushfires. *Remote*

27 *Sensing*, *13*(16), 3092, 2021

28 Bègue, N., Vignelles, D., Berthet, G., Portafaix, T., Payen, G., Jégou, F., Bencherif, H., Jumelet,

29 J., Vernier, J. P., Lurton., T., Renard, J. B., Clarisse., L., Duverger, V., Posny, F., Metzger, J.

30 M., and Godin-Beekmann, S.: Long-range isentropic transport of stratospheric aerosols over

31 Southern Hemisphere following the Calbuco eruption in April 2015, 15019–15036,

32 https://doi.org/10.5194/acp-17-15019-2017, 2017.

1 Bencherif, H., El Amraoui, L., Kirgis, G., Leclair De Bellevue, J., Hauchecorne, A., Mzé, N.,

2 Portafaix, T., Pazmino, A., and Goutail, F.: Analysis of a rapid increase of stratospheric ozone

3 during late austral summer 2008 over Kerguelen (49.4° S, 70.3° E), Atmos. Chem. Phys., 11,

4 363–373, https://doi.org/10.5194/acp-11-363-2011, 2011

5 Boers, R., A. T. de Laat, D. C. Stein Zweers, and R. J. Dirksen: Lifting potential of solar-heated

6 aerosol layers, Geophys. Res. Lett., 37, L24802, doi:10.1029/2010GL045171, 2010

7 Burton, S.P., Hair, J.W., Kahnert, M., Ferrare, R.A., Hostetler, C.A., Cook, A.L., Harper, D.B.,

8 Berkoff, T.A., Seaman, S.T., Collins, J.E., Fenn, M.A., Rogers, R.R., 2015. Observations of the

9 spectral dependence of linear particle depolarization ratio of aerosols using NASA Langley

10 airborne High Spectral Resolution Lidar. Atmos. Chem. Phys. 15, 13453–13473.

11 https://doi.org/10.5194/acp-15-13453-2015

12 Cai, D., Abram, N. J., Sharples, J. J. and Perkins-Kirkpatrick, S. E. (2022). Increasing intensity

13 and frequency of cold fronts contributed to Australia's 2019–2020 Black Summer fire

14 disaster. *Environmental Research Letters*, *17*(9), 094044.

15 Campanelli, M., Estelles, V., Tomasi, C., Nakajima, T., Malvestuto, V., and Martinez-Lozano,

16 J. A.: Application of the SKYRAD improved Langley plot method for the in-situ calibration of

17 CIMEL sun-sky photometers, Appl. Optics, 46, 2688–2702, 2007.

18 Che, H., Shi, G., Uchiyama, A., Yamazaki, A., Chen, H., Goloub, P., and Zhang, X.:

19 Intercomparison between aerosol optical properties by a PREDE skyradiometer and CIMEL

20 sunphotometer over Beijing, China, Atmos. Chem. Phys., 8, 3199–3214, doi:10.5194/acp-8-

21 3199-2008, 2008.

22 Clain, G., Baray, J. L., Delmas, R., Diab, R., Leclair de Bellevue, J., Keckhut, P., Posny, F.,

23 Metzger, J. M., and Cammas, J. P.: Tropospheric ozone climatology at two Southern

24 Hemisphere tropical/subtropical sites, (Reunion Island and Irene, South Africa) from

25 ozonesondes, LIDAR, and in situ aircraft measurements, 9, 1723–1734,

26 https://doi.org/10.5194/acp-9-1723-2009, 2009

27 Clerbaux, C., Boynard, A., Clarisse, L., George, M., Hadji-Lazaro, J., Herbin, H., Hurtmans,

28 D., Pommier, M., Razavi, A., Turquety, S: Monitoring of atmospheric composition using the

29 thermal infrared IASI/MetOp sounder, Atmos. Chem. Phys. 2009, 9, 6041–6054, 2009.

30 Coheur, P.-F., Clarisse, L., Turquety, S., Hurtmans, D., and Clerbaux, C.: IASI measurements

31 of reactive trace species in BB plumes, Atmos. Chem. Phys., 9, 5655–5667, doi:10.5194/acp-

32 9-5655-2009, 2009.

1 De Laat, A.T.J.; Stein Zweers, D.C.; Boers, R.; Tuinder, O.N. A solar escalator: Observational

2 evidence of the self-lifting of smoke and aerosols by absorption of solar radiation in the

3 February 2009 Australian Black Saturday plume. J. Geophys. Res. Atmos. 2012, 117.

4 Dowdy, A. J and Pepler, A: Pyroconvection risk in Australia: Climatological changes in

5 atmospheric stability and surface fire weather conditions. Geophysical Research Letters, 45,

6 2005–2013. https://doi.org/10.1002/2017GL076654, 2018

7 Duflot, V., Royer, P., Chazette, P., Baray, J. L., Courcoux, Y. and Delmas, R.: Marine and BB

8 aerosols in the southern Indian Ocean: Retrieval of aerosol optical properties from shipborne

9 lidar and Sun photometer measurements. *Journal of Geophysical Research:*

10 *Atmospheres*, *116*(D18), 2011

11 Duflot, V., Bègue, N., Pouliquen, M. L., Goloub, P. and Metzger, J. M : Aerosols on the

12 Tropical Island of La Réunion (21° S, 55° E): Assessment of Climatology, Origin of Variability

13 and Trend. *Remote Sensing*, *14*(19), 4945, 2022

14 Fromm, M., Lindsey, D. T., Servranckx, R., Yue, G., Trickl, T., Sica, R.: The untold story of

15 pyro-cumulonimbus. Bulletin of the American Meteorological Society, 91(9), 2010

16 Hamill, P., Jensen, E. J., Russell, P. B., and Bauman, J. J.: The life cycle of stratospheric aerosol

17 particles, B. Am. Meteorol. Soc., 78, 1395–1410, https://doi.org/10.1175/1520-

18 0477(1997)078E2.0.CO;2, 1997

19 Haarig, M.; Ansmann, A.; Baars, H.; Jimenez, C.; Veselovskii, I.; Engelmann, R.; Althausen,

20 D. Depolarization and lidar ratios at 355, 532, and 1064 nm and microphysical properties of

21 aged tropospheric and stratospheric Canadian wildfire smoke. Atmos. Chem. Phys. 2018, 18,

22 11847–11861.

23 Hashimoto, M., Nakajima, T., Dubovik, O., Campanelli, M., Che, H., Khatri, P., Takamura, T

24 and Pandithurai, G: Development of a new data-processing method for SKYNET sky

25 radiometer observations. *Atmospheric Measurement Techniques*, *5*(11), 2723-2737, 2012

26 Hauchecorne, A., Godin, S., Marchand, M., Heese, B., and Souprayen, C.: Quantification of

27 the transport of chemical constituents from the polar vortex to midlatitudes in the lower

28 stratosphere using the high-resolution advection model MIMOSA and effective diffusivity, J.

29 Geophys. Res.-Atmos., 107, 1–13, 2002

30 Héron, D., Evan, S., Brioude, J., Rosenlof, K., Posny, F., Metzger, J. M., & Cammas, J. P.:

31 Impact of convection on the upper-tropospheric composition (water vapor and ozone) over a

1 subtropical site (Réunion island; 21.1° S, 55.5° E) in the Indian Ocean. *Atmospheric Chemistry*
2 *and Physics*, *20*(14), 8611-8626., 2020

3 Heese, B., Godin, S., and Hauchecorne, A.: Airborne lidar measurements of ozone filaments
4 during METRO–A validation of PV advection model MIMOSA, J. Geophys. Res, 106, 20011–
5 20024, 2001.

6 Hu, Q., Goloub, P., Veselovskii, I., Bravo-Aranda, J.-A., Popovici, I. E., Podvin, T., Haeffelin,
7 M., Lopatin, A., Dubovik, O., Pietras, C., Huang, X., Torres, B., and Chen, C.: Long-range-
8 transported Canadian smoke plumes in the lower stratosphere over northern France, Atmos.
9 Chem. Phys., 19, 1173–1193, https://doi.org/10.5194/acp-19-1173-2019, 2019.

10 Hurtmans, D., Coheur, P.F.; Wespes, C., Clarisse, L., Scharf, O., Clerbaux, C., Hadji-Lazaro,
11 J., George, M., Turquety, S: FORLI radiative transfer and retrieval code for IASI. J. Quant.
12 Spectrosc. Radiat. Transf. 2012, 113, 1391–1408, 2012

13 Jäger, H. and Deshler, T.: Lidar backscatter to extinction, mass and area conversions for
14 stratospheric aerosols based on midlatitude balloon borne size distribution measurements,
15 Geophys. Res. Lett., 29, 1929, https://doi.org/10.1029/2002GL015609, 2002

16 Jones, N. B., Rinsland, C. P., Liley, J. B., and Rosen, J.: Correlation of aerosol and carbon
17 monoxide at 45 S: Evidence of BB emissions. *Geophysical research letters, 28(4), 709-712.,*
18 *2001*

19 Kablick III, G. P., Allen, D. R., Fromm, M. D. and Nedoluha, G. E: Australian pyroCb smoke
20 generates synoptic-scale stratospheric anticyclones, Geophys. Res. Let., 47(13),
21 e2020GL088101, 2020.

22 Khaykin, S., Legras, B., Bucci, S., Sellitto, P., Isaksen, L., Tence, F. and Godin-Beekmann, S:
23 The 2019/20 Australian wildfires generated a persistent smoke-charged vortex rising up to 35
24 km altitude. Communications Earth & Environment, 1(1), 1-12, 2020.

25 Khaykin, S. M., Godin-Beekmann, S., Hauchecorne, A., Pelon, J., Ravetta, F., and Keckhut, P:
26 Stratospheric smoke with unprecedentedly high backscatter observed by lidars above southern
27 France, Geophys. Res. Lett., 1944, 8007, doi:10.1002/2017GL076763, 2018.

28 Klett, J. D.: Lidar inversion with variable backscatter/extinction ratios, Appl. Opt., AO, 24,
29 1638–1643, https://doi.org/10.1364/AO.24.001638, 1985.

30 Kloss, C.; Sellitto, P., Von Hobe, M.; Berthet, G.; Smale, D.; Krysztofiak, G.; Legras, B.
31 Australian fires 2019–2020: Tropospheric and stratospheric pollution throughout the whole fire
32 season. Front. Environ. Sci. 2021, 9, 220, 2021

1 Kloss, C., Berthet, G., Sellitto, P., Ploeger, F., Bucci, S., Khaykin, S., Jégou, F., Taha, G.,

2 Thomason, L. W., Barret, B., Le Flochmoen, E., von Hobe, M., Bossolasco, A., Bègue, N., and

3 Legras, B.: Transport of the 2017 Canadian wildfire plume to the tropics via the Asian monsoon

4 circulation, Atmos. Chem. Phys., 19, 13547–13567, https://doi.org/10.5194/acp-19-13547-

5 2019, 2019.

6 Kloss, C., Sellitto, P., Renard, J. B., Baron, A., Bègue, N., Legras, B., Berthet., G., Briaud., E.,

7 Carboni., E., Duchamp., C., Duflot., V., Jacquet., P., Marquestaut., N., Metzger. J-M., Payen.,

8 G., Ranaivombola., M., Roberts., T., Siddans., R. and Jegou, F.: Aerosol characterization of the

9 stratospheric plume from the volcanic eruption at Hunga Tonga 15 January 2022. *Geophysical*

10 *Research Letters*, *49*(16), e2022GL099394., 2022

11 Kremser, S., Thomason, L. W., Hobe, M., et al.: Stratospheric aerosol – Observations,

12 processes, and impact on climate, Rev. Geophys., 54, 278–335, 2016.

13 Labonne, M., Bréon, F. M., & Chevallier, F.: Injection height of BB aerosols as seen from a

14 spaceborne lidar. *Geophysical Research Letters*, *34*(11), 2007

15 Levin, N., Yebra, M. and Phinn, S.: Unveiling the factors responsible for Australia's Black

16 Summer fires of 2019/2020. *Fire*, *4*(3), 58, 2021

17 Livesey, N., Read, W., Wagner, P., Froidevaux, L., Santee, M., Schwartz, M., et al.: Earth

18 Observing System (EOS): Aura Microwave Limb Sounder (MLS): Version 5.0x Level 2 and 3

19 Data Quality and Description Document. Jet Propulsion Lab. JPL. D-105336 Rev. A, 2020

20 de Mazière, M. D., Thompson, A. M., Kurylo, M. J., Wild, J. D., Bernhard, G., Blumenstock,

21 T. and Strahan, S. E: The Network for the Detection of Atmospheric Composition Change

22 (NDACC): history, status and perspectives, Atmos. Chem. Phys., 18(7), 4935-4964, 2018

23 Müller, D., Ansmann, A., Mattis, I., Tesche, M., Wandinger, U., Althausen, D., and Pisani, G.:

24 Aerosol-type-dependent lidar ratios observed with Raman lidar, J. Geophys. Res., 112, D16202,

25 https://doi.org/10.1029/2006JD008292, 2007

26 Nakajima, T., Tonna, G., Rao, R., Kaufman, Y., and Holben, B.: Use of sky brightness

27 measurements from ground for remote sensing of particulate polydispersions. Appl. Optics, 35,

28 2672–2686, 1996

29 Neumann, C.: Global guide to tropical cyclone forecasting, WMO Trop. Cyclone Program Rep.

30 TCP-31, chap. Global Overview, World Meteorol. Organ., Geneva, Switzerland, 43 pp., 1993

1 Nicolae, D., Nemuc, A., Müller, D., Talianu, C., Vasilescu, J., Belegante, L. and Kolgotin, A.

2 : Characterization of fresh and aged BB events using multiwavelength Raman lidar and mass

3 spectrometry. *Journal of Geophysical Research: Atmospheres*, *118*(7), 2956-2965, 2013

4 Ohneiser, K., Ansmann, A., Chudnovsky, A., Engelmann, R., Ritter, C., Veselovskii, I., Baars,

5 H., Gebauer, H., Griesche, H., Radenz, M., Hofer, J., Althausen, D., Dahlke, S., and Maturilli,

6 M.: The unexpected smoke layer in the High Arctic winter stratosphere during MOSAiC 2019–

7 2020, Atmos. Chem. Phys., 21, 15783–15808, https://doi.org/10.5194/acp-21-15783-2021,

8 2021.

9 Pisso, I., Sollum, E., Grythe, H., Kristiansen, N. I., Cassiani, M., Eckhardt, S., Arnold, D.,

10 Morton, D., Thompson, R. L., Groot Zwaaftink, C. D., Evangeliou, N., Sodemann, H.,

11 Haimberger, L., Henne, S., Brunner, D., Burkhart, J. F., Fouilloux, A., Brioude, J., Philipp, A.,

12 Seibert, P., and Stohl, A.: The Lagrangian particle dispersion model FLEXPART version 10.4,

13 Geosci. Model Dev., 12, 4955–4997, https://doi.org/10.5194/gmd-12-4955-2019, 2019.

14 Portafaix, T., Morel, B., Bencherif, H., Baldy, S., Godin-Beekmann, S., and Hauchecorne, A.:

15 Fine-scale study of a thick stratospheric ozone lamina at the edge of the southern subtropical

16 barrier, J. Geophys. Res.-Atmos., 108, D64196, https://doi.org/10.1029/2002JD002741, 2003.

17 Pumphrey, H. C., Filipiak, M. J., Livesey, J., Scwartz, M. J., Boone, C., Walker, K. A., Bernath,

18 P., Ricaud, P., Barret, B., Clerbaux, C., Jarnot, R. F., Manney, G. L. and Waters, J. W:

19 Validation of middle-atmosphere carbon monoxide retrievals from the Microwave Limb

20 Sounder on Aura, J. Geophys. Res., 112, D24S38, doi: 10.1029/2007JD008723, 2007.

21 Sakai, T., T. Nagai, M. Nakazato, Y. Mano, and T. Matsumura: Ice clouds and Asian dust

22 studied with lidar measurements of particle extinction-to-backscatter ratio, particle

23 depolarization, and water vapor mixing ration over Tsukuba. Applied Optics 42 7103 –7116,

24 2003

25 Sakai, T., O. Uchino, T. Nagai, B. Liley, I. Morino, and T. Fujimoto: Long-term variation of

26 stratospheric aerosols observed with lidars over Tsukuba, Japan, from 1982 and Lauder, New

27 Zealand, from 1992 to 2015, J. Geophys. Res. Atmos., 121, 10,283–10,293,

28 doi:10.1002/2016JD025132, 2016

29 Schoeberl, M. R., Douglass, A. R., Hilsenrath, E., Bhartia, P. K.,Barnett, J., Beer, R., Waters,

30 J., Gunson, M., Froidevaux, L.,Gille, J., Levelt, P. F., and DeCola, P.: Overview of the EOS

31 Aura Mission, IEEE Trans. Geosci. Remote Sens., 44, 1066–1074, 2006.

1 Sellitto, P., Podglajen, A., Belhadji, R., Boichu, M., Carboni, E., Cuesta, J., C. Duchamp, C.

2 Kloss, R. Siddans, N. Bègue, L. Blarel, F. Jegou, S. Khaykin, J. -B. Renard. and Legras, B.:

3 The unexpected radiative impact of the Hunga Tonga eruption of 15th January

4 2022. *Communications Earth & Environment*, *3*(1), 1-10., 2022

5 Taha, G., Loughman, R., Zhu, T., Thomason, L., Kar, J., Rieger, L. and Bourassa, A: OMPS

6 LP Version 2.0 multi-wavelength aerosol extinction coefficient retrieval algorithm.,

7 *Atmospheric Measurement Techniques*, *14*(2), 1015-1036, 2021

8 Tencé, F., Jumelet, J., Bekki, S., Khaykin, S., Sarkissian, A. and Keckhut, P.: Australian Black

9 Summer smoke observed by lidar at the French Antarctic station Dumont d'Urville. *Journal of*

10 *Geophysical Research: Atmospheres*, *127*(4), e2021JD035349, 2022

11 Turquety, S., Menut, L., Siour, G., Mailler, S., Hadji-Lazaro, J., George, M., Clerbaux, C.,

12 Hurtmans, D., Coheur, P.-F: APIFLAME v2.0 BB emissions model: Impact of refined input

13 parameters on atmospheric concentration in Portugal in summer 2016. Geosci. Model. Dev.,

14 2020, 13, 2981–3009, 2020.

15 Uchino, O., Tokunaga, M., Seki, K., Maeda, M., Naito, K., and Takahashi, K: Lidar

16 measurement of stratospheric transmission at a wavelength of 340 nm after the eruption of El

17 Chichon, J. Atmos. Terr. Phys., 45, 12, 849–850, 1983

18 Vernier, J. P., Pommereau, J. P., Garnier, A., Pelon, J., Larsen, N., Nielsen, J., and McDermid,

19 I. S., Tropical stratospheric aerosol layer from CALIPSO lidar observations, J. Geophys. Res.-

20 Atmos., 114, D00H10, https://doi.org/10.1029/2009JD011946, 2009

21 Wunch, D., Toon, G. C., Sherlock, V., Deutscher, N. M., Liu, C., Feist, D. G., and Wennberg,

22 P. O.: The Total Carbon Column Observing Network's GGG2014 Data Version, p. 43,

23 https://doi.org/10.14291/tccon.ggg2014.documentation.R0/122, 2015.

24 Young, S.A.: Analysis of lidar backscatter profiles in optically thin clouds, Appl. Opt., 34,

25 7019–7031., 1995

26 Yu, P.; Davis, S.M.; Toon, O.B.; Portmann, R.W.; Bardeen, C.G.; Barnes, J.E.; Telg, H.;

27 Maloney, C.; Rosenlof, K.H. Persistent Stratospheric Warming due to 2019–2020 Australian

28 Wildfire Smoke. Geophys. Res. Lett. 2020, 2020, e2021GL092609, 2020

29 Yu, P., Davis, S. M., Toon, O. B., Portmann, R. W., Bardeen, C. G., Barnes, J. E., ... & Rosenlof,

30 K. H: Persistent stratospheric warming due to 2019–2020 Australian wildfire

31 smoke. *Geophysical Research Letters*, *48*(7), e2021GL092609, 2021

1 Zhou, M., Langerock, B., Vigouroux, C., Sha, M. K., Ramonet, M., Delmotte, M., ... & De

2 Mazière, M.: Atmospheric CO and CH 4 time series and seasonal variations on Reunion Island

3 from ground-based in situ and FTIR (NDACC and TCCON) measurements. *Atmospheric*
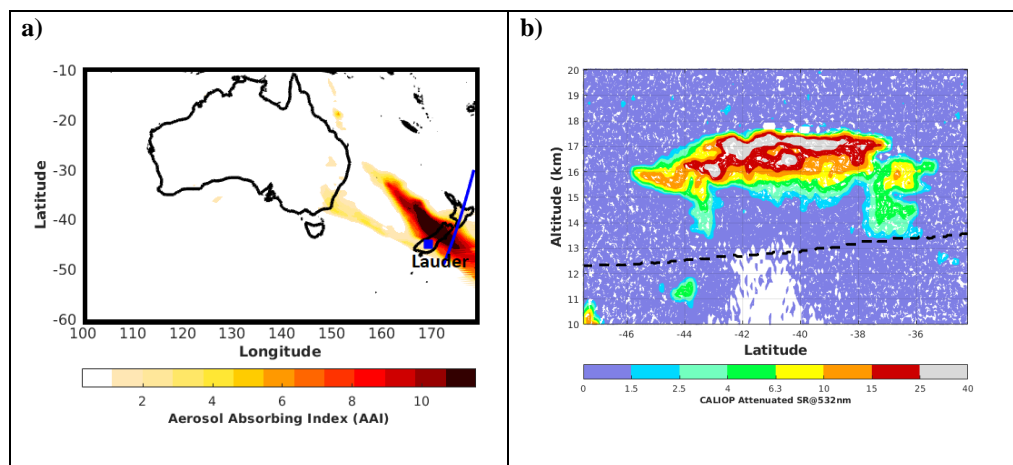
4 *Chemistry and Physics*, *18*(19), 13881-13901, 2018

5

1

2 **FIGURES AND TABLE**

3

4

5

6 **Figure 1: (a)** Map of Aerosol Absorbing Index obtained from OMPS observations and **(b)**
7 scattering ratio profiles at 532 nm obtained from CALIOP observations on 1st January 2020.
8 The orbit overpass of CALIOP is indicated by the blue curve, while the blue square corresponds
9 to the Lauder site in plot (a). The black dashed line in (b) corresponds to the 380 K isentropic
10 level calculated from CALIOP observations.
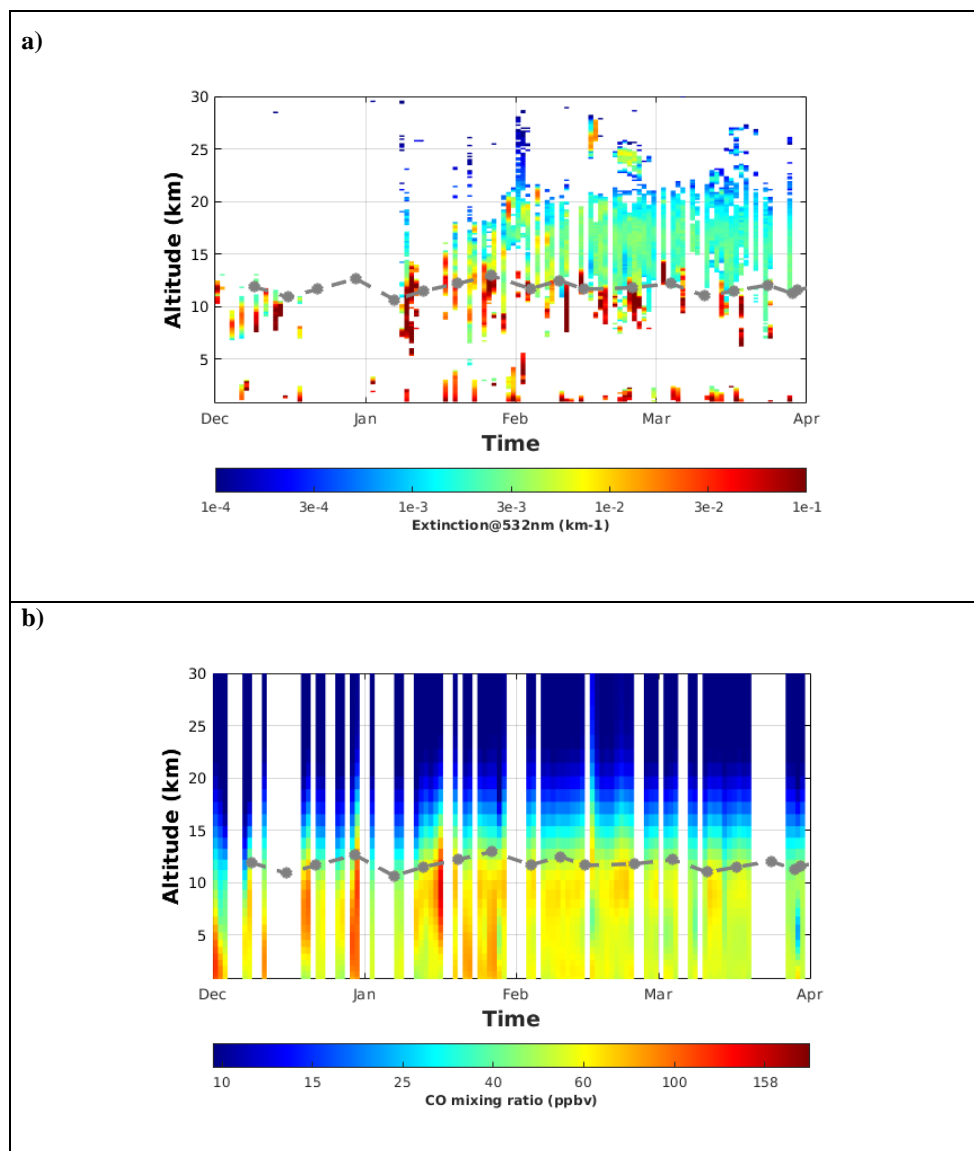
11

Figure 2: Time series of daily profiles at Lauder of (a) aerosol extinction at 532 nm obtained from lidar and (b) CO mixing ratio obtained from FTIR between 1st December 2019 and 1st April 2020. In order to screen non-aerosol contributors (such as clouds) on the extinction measurements, a mask based on the method reported by Nicolae et al. (2013) that includes consideration on plausible aerosols properties was used. Namely, we only kept profile parts with positive depolarization values, and Angström exponent ranges from 0.1 to 4. The grey line indicates the tropopause height obtained from radiosonde measurements.

1
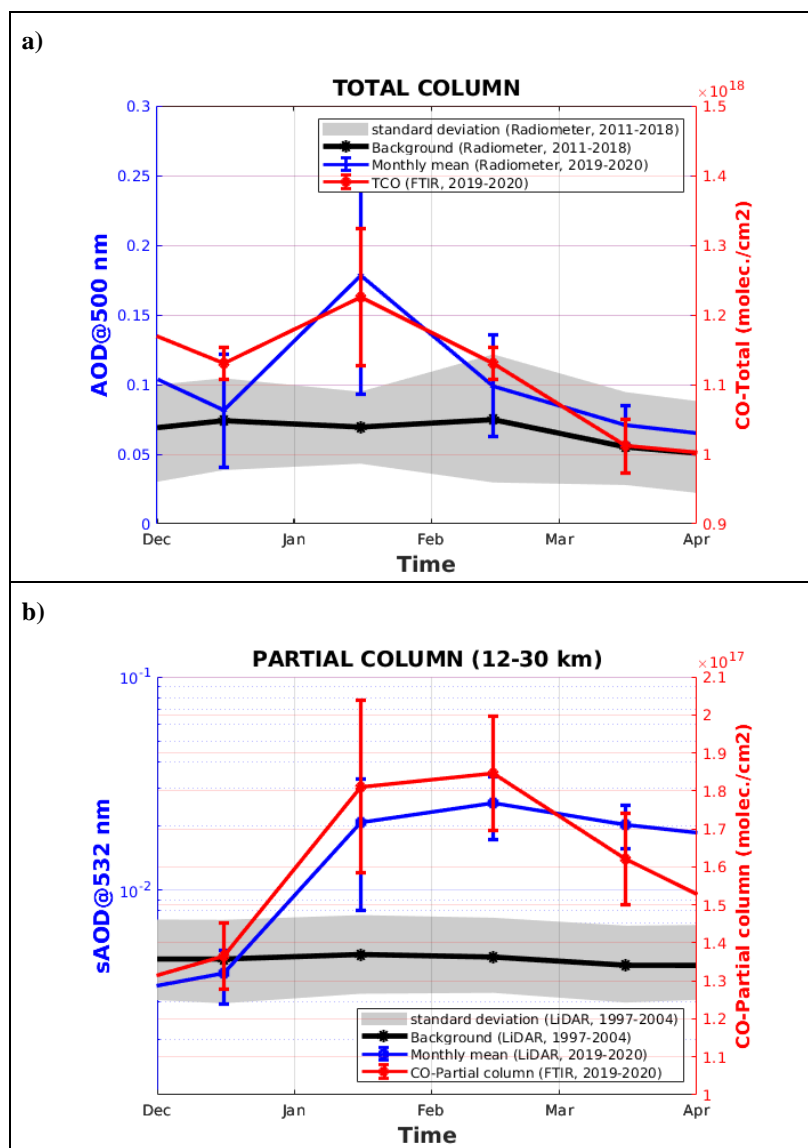
Figure 3: (a) Monthly mean evolution of total column of aerosol (AOD at 500 nm) and CO obtained from SKYNET radiometer and FTIR respectively over Lauder from 1st December 2019 to 1st April 2020. **(b)** Monthly mean evolution of the stratospheric AOD (sAOD) and CO (sCO) columns at Lauder between 1st December 2019 and 1st April 2020. The sAOD and sCO are calculated between 12 and 30 km from lidar and FTIR measurements respectively. The background evolution of aerosol data (AOD: 2011-2018 and sAOD: 1997-2004) and the associated standard deviation are given in black lines and grey areas, respectively.

1

2
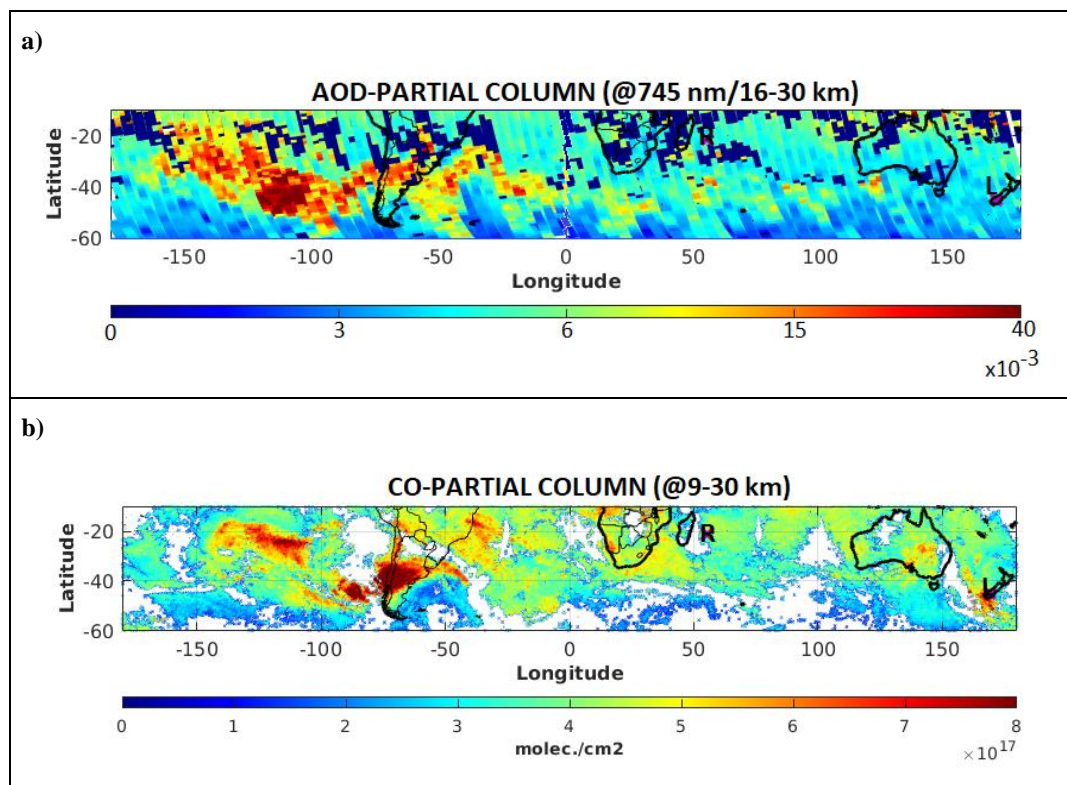
Figure 4: Time-averaged map (from 9th to 16th January 2020) of (a) sAOD (between 16 and 30 km at 745 nm) obtained from OMPS observations and (b) partial column of CO (averaged between 9 and 30 km) obtained from IASI observations. The location of Reunion and Lauder sites are indicated by R and L respectively.

7
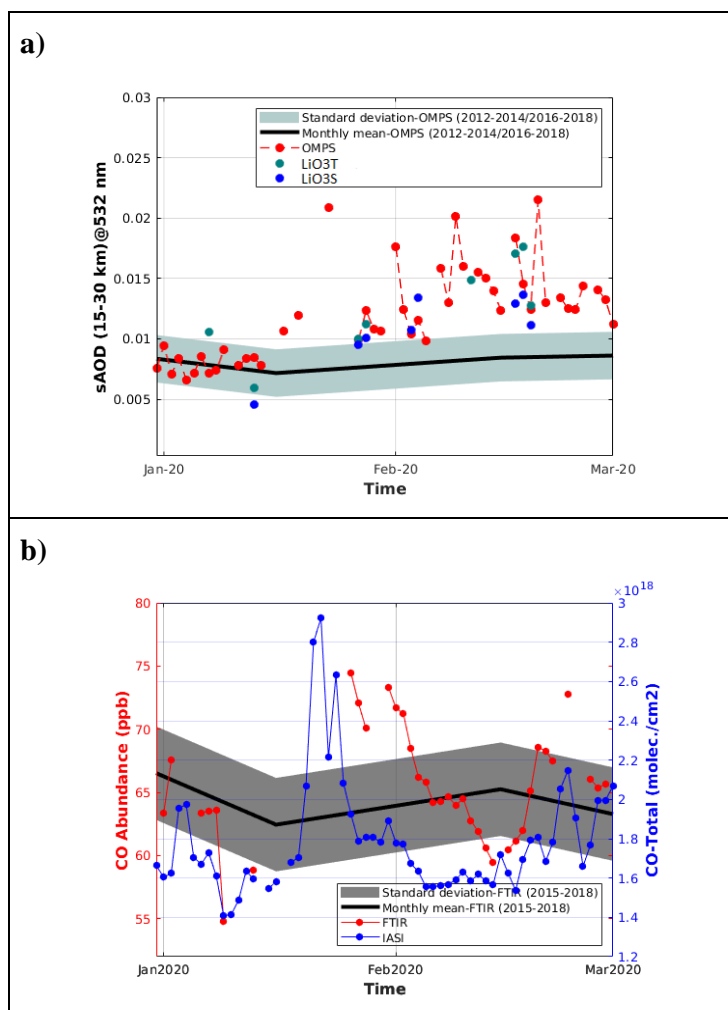
Figure 5: Daily mean evolution of aerosol (a) and CO (b) abundances obtained from ground-based and satellite observations at Reunion between 1st January and 1st March 2020. Total column (molecule.cm^{-2}) and abundance (ppb) of CO obtained from IASI (blue line) and FTIR (red line) respectively are given in the lower panel (b), while sAOD obtained from OMPS (red line) and Lidar (blue and green dots) are given in the upper panel (a). The black and dashed lines correspond to monthly mean and the associated standard deviation calculated during the background period.
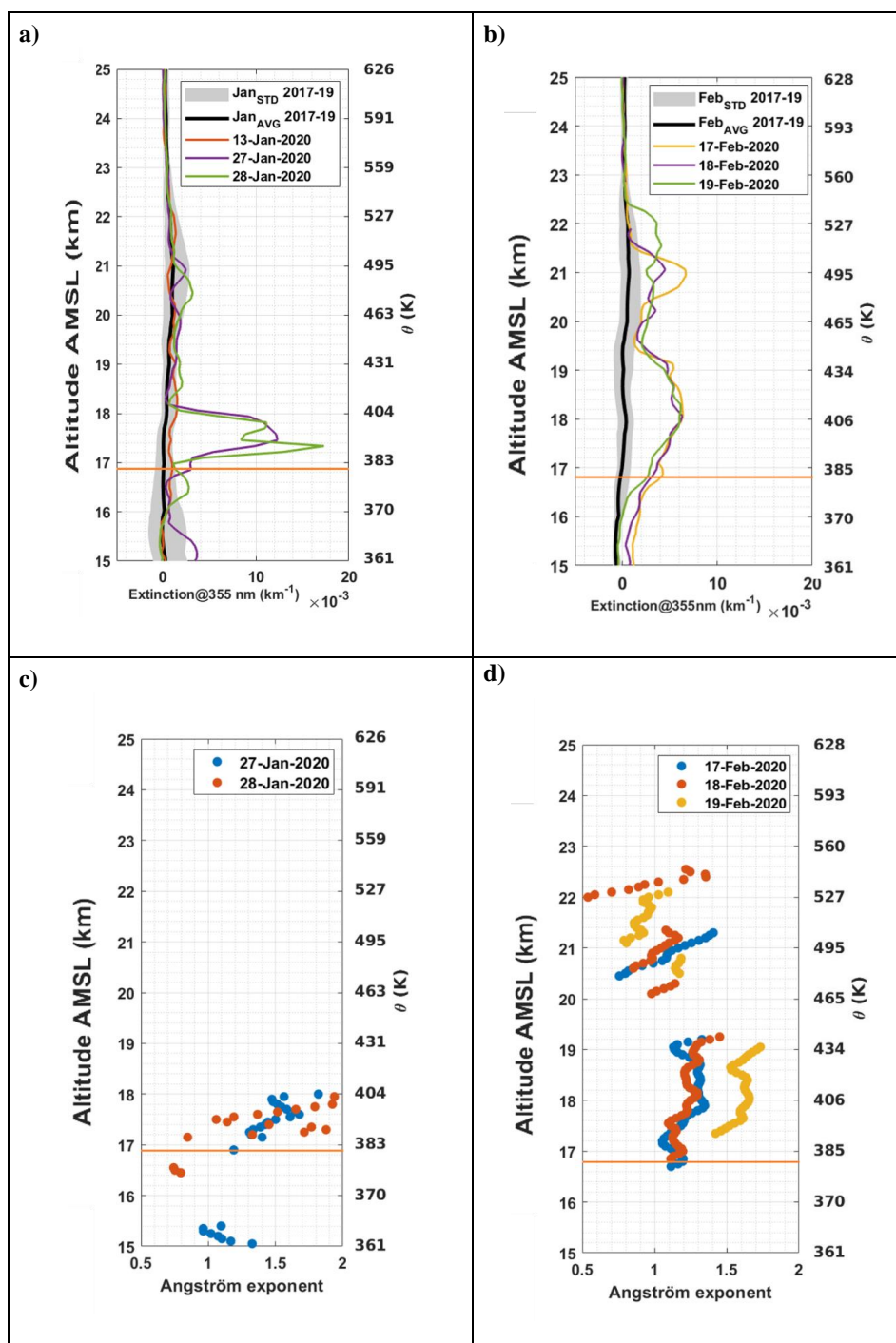
Figure 6: Aerosol extinction (at 355 nm) (a, b) and Angström exponent (355-532 nm) (c, d) obtained from lidar observations at Reunion in the months January and February 2020. The tropopause height is indicated by the orange horizontal lines.

1
2
3
4
5
6
7
8
9
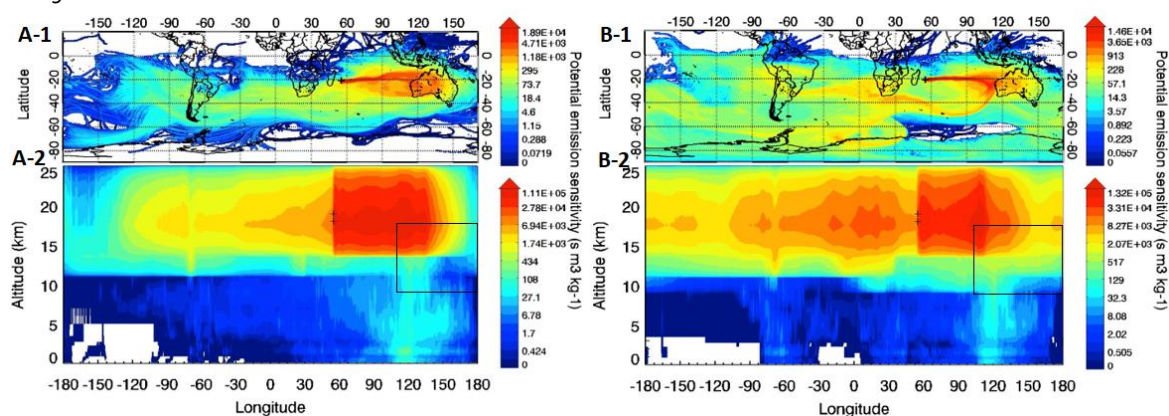
Figure 7: FLEXPART 30-day back trajectories initialized from Reunion (black cross) at 18 km on 27th January 2020 (A-1-2) and 28th January 2020 (B-1-2). A-1 and B-1 correspond to an integration of the trajectory positions over the whole altitude range. A-2 and B-2 are the vertical view integrated over the whole latitude range of the back trajectories A-1 and B-1. The black rectangle represented the injection height of the biomass burning aerosols.

16
17
18

1
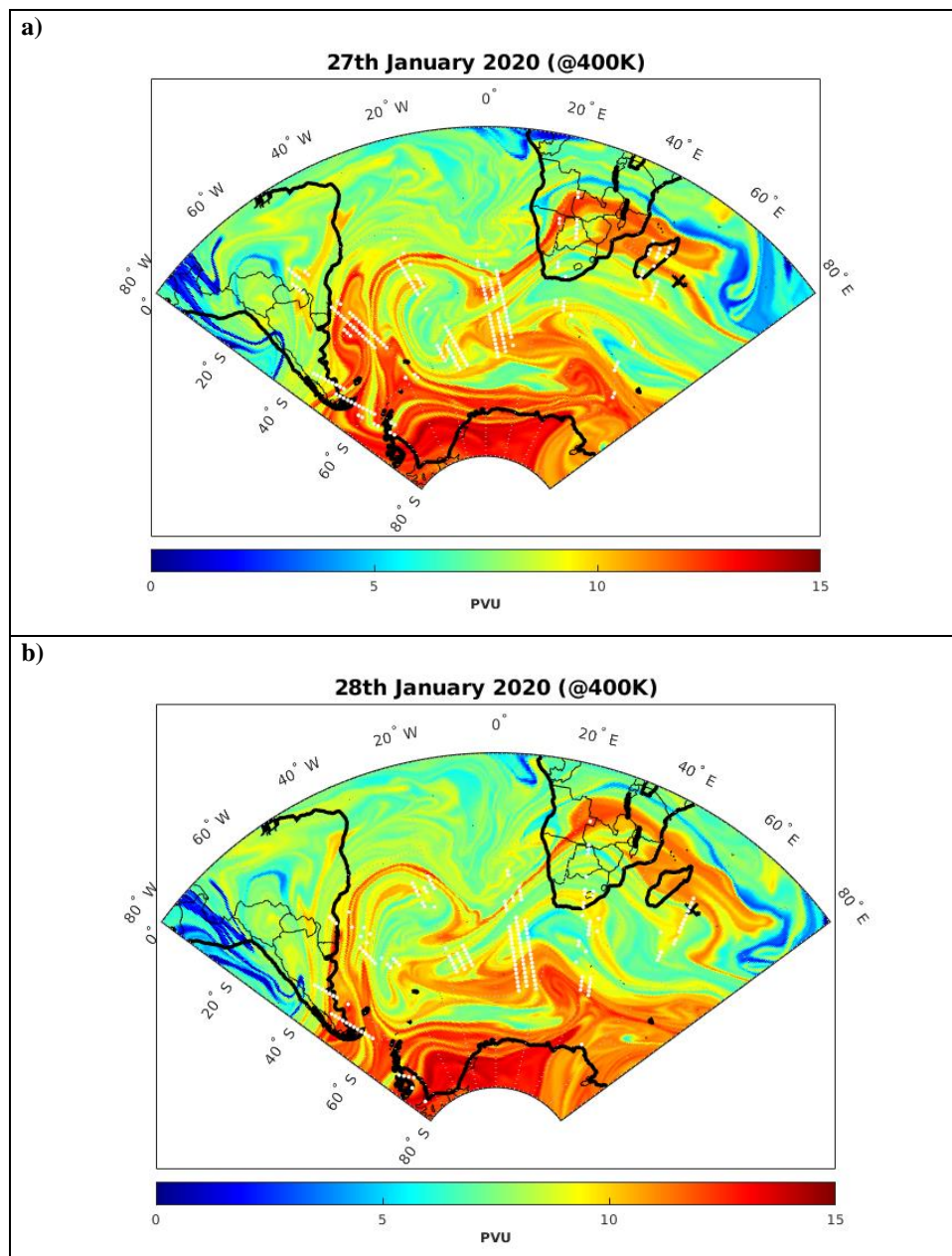
Figure 8: Advected PV map at the 400 K level obtained from the MIMOSA model (a) on 27 January 2022 and (b) on 28 January 2022. The white dots represent the localization of the aerosol plume at 400 K ± 5 K obtained from OMPS observations, while the black cross indicates Reunion.
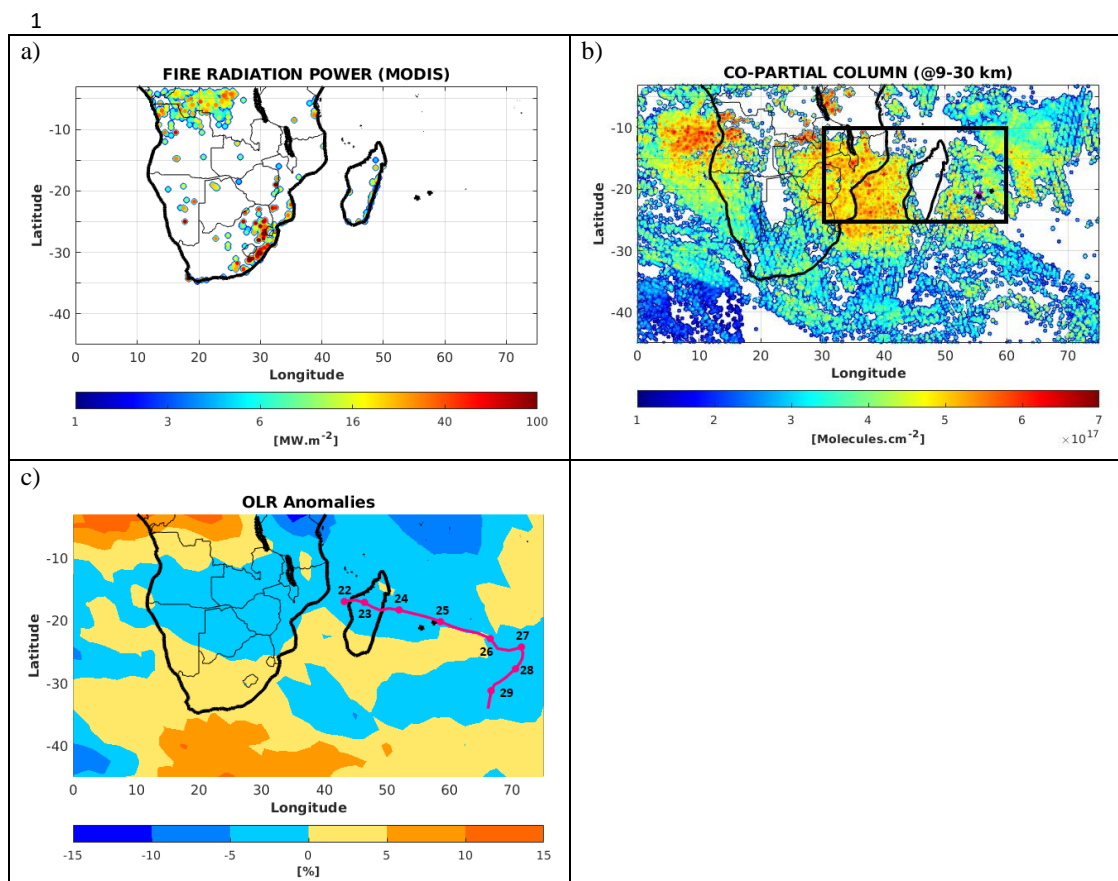
6

1

2

3

4

5

6

7

8
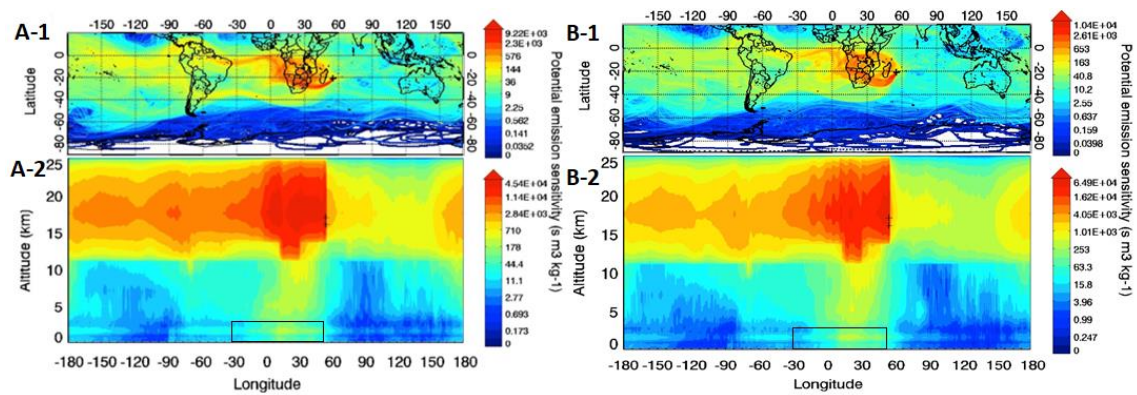
10 **Figure 9:** Same as figure 7 with an injection height initialized at 16 km.

11

12

1

2 **Figure 10:** a) The total number of fire pixel and the associated fire radiative power obtained
3 from MODIS observation between 16th and 29th January 2020. b) Time-average map of partial
4 column of CO (calculated between 9 and 30 km) obtained from IASI observations averaged
5 between 16th and 29th January 2020. The black square corresponds to the study domain where
6 the vertical cross-section of CO and water vapor mixing ratio are calculated and reported in
7 Figure 11. c) Time-average map of outgoing longwave radiation anomalies obtained from
8 NCEP between 16th and 29th January 2020. The red curve corresponds the trajectory followed
9 by the Diane strong tropical storm from 22nd to 29th January 2020. This trajectory is obtained
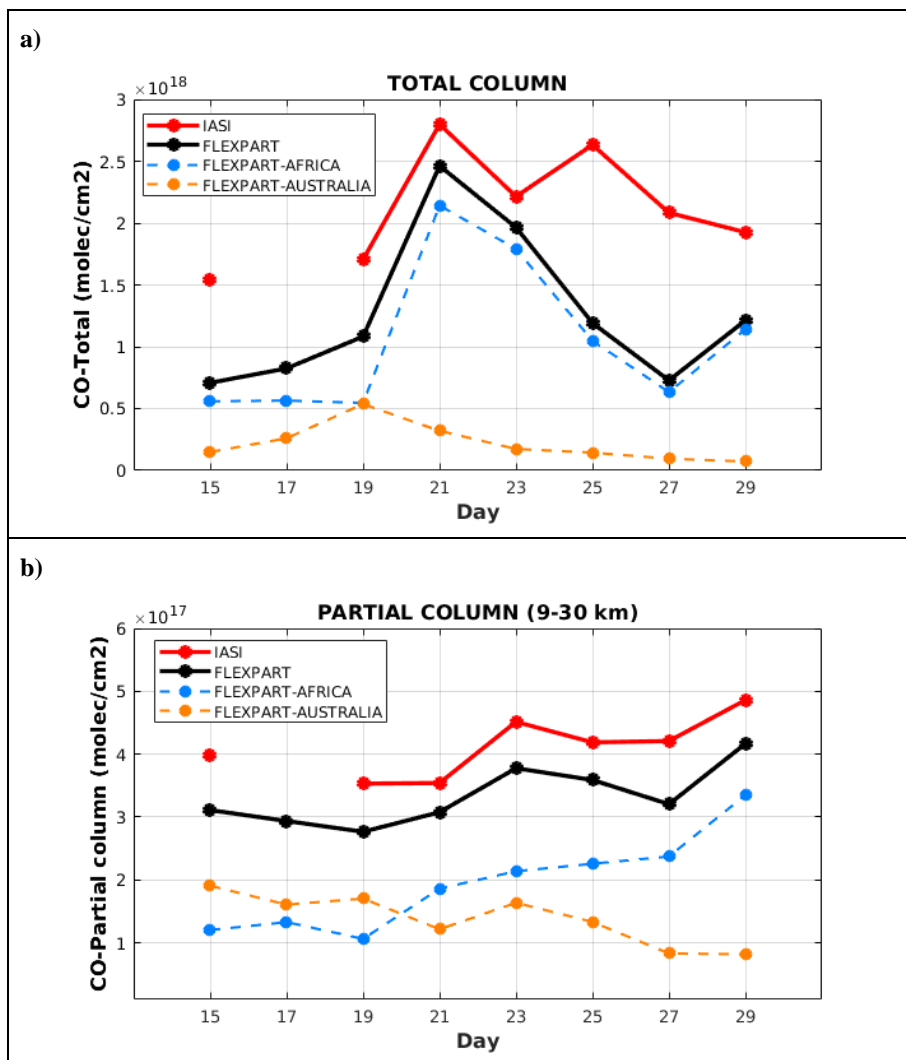10 from the RSMC (Regional Specialized Meteorological Center) of Reunion best-track database.
11
12

1

2
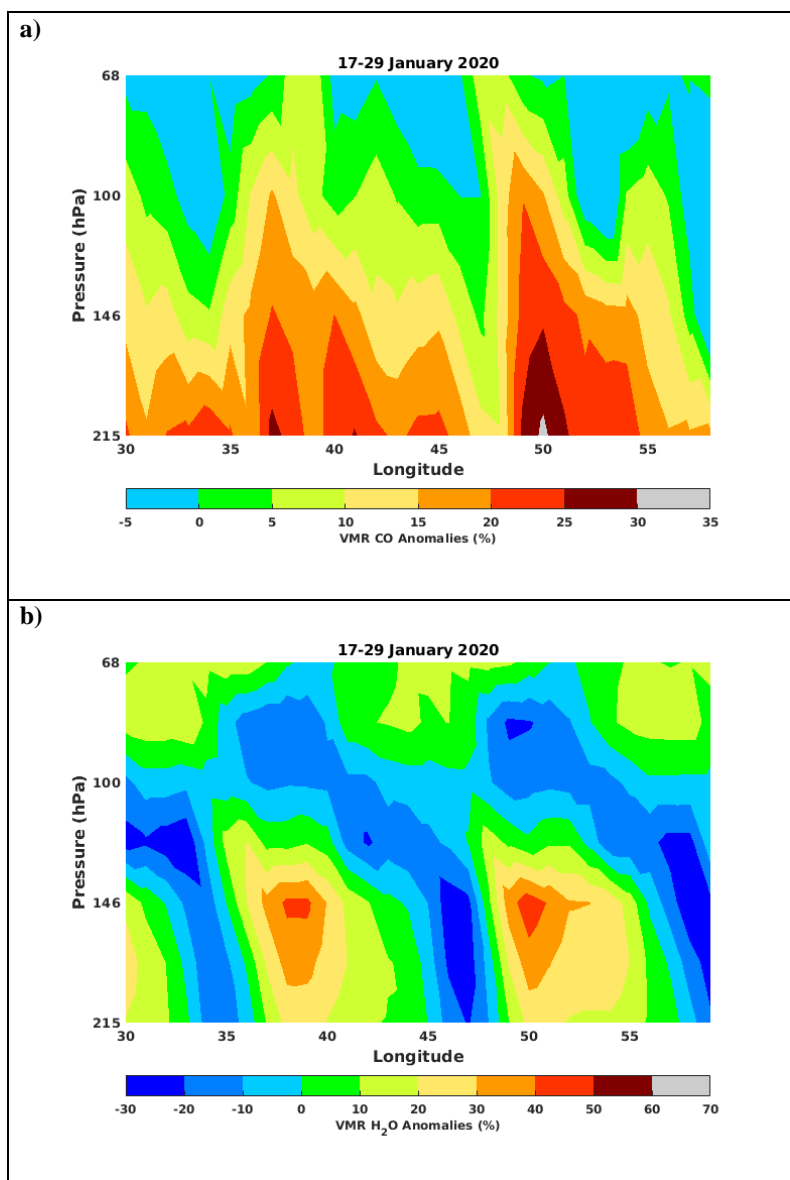
Figure 11: Vertical cross section of (a) CO and (b) water vapor mixing ratio anomalies obtained from MLS observation over southern Africa and the SWIO basin (black box in Figure 10b) between 16th and 29th January 2020.

6

1

Figure 12: Daily evolution of (a) total column and (b) partial column (calculated between 9 and 30 km) of CO observed by IASI (red line) and simulated by FLEXPART (black line) over Reunion from 15ᵗʰ to 29ᵗʰ January 2020. The CO evolution is simulated by FLEXPART in considering only the CO emission (including BB and anthropogenic activity) from African (cyan line) and Australian (orange line) BB sources.

7

1

2

3
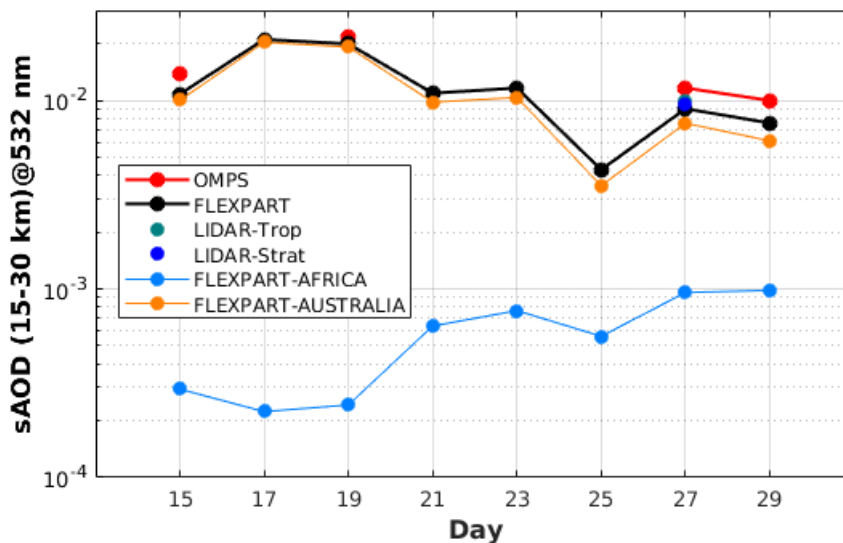
Figure 13: Daily evolution of sAOD (calculated between 15 and 30 km at 532 nm) obtained from OMPS (red line), lidar (blue dots) and simulated by FLEXPART (black line) over Reunion from 15th to 29th January 2020. The simulated sAOD are calculated in considering only the aerosol emission (BC and OC) from African (cyan line) and Australian (orange line) BB sources.

9